Alma Mater Studiorum · University of Bologna

School of Science
Department of Physics and Astronomy
Master Degree in Physics

ELECTROPRODUCTION OF HYPERNUCLEI

Supervisor:
Prof. Paolo Finelli

Submitted by:
Martina Pepiciello

Co-supervisors:
Prof. Carlotta Giusti
Dr. Matteo Vorabbi

Academic Year 2020/2021

Abstract

Hypernuclear spectroscopy has received considerable attention lately, because it is an essential tool for the study of the hyperon-nucleon interaction; this, in turn, is believed to play an important role in dense nuclear matter, such as neutron star interiors. In particular, the current experimental research is focusing on $(e, e'K)$ reactions on various nuclear targets, with an extensive measurement program being carried out at Jefferson National Laboratory. With the aim of contributing to the theoretical understanding of electroproduction of hypernuclei, we develop a formalism for the evaluation of triple differential cross sections using the impulse approximation. We also develop a Python program for the numerical calculation of these cross sections, and we present our results for the unpolarized triple differential cross section of the $e + {}^{12}C \to e' + K + {}^{12}_{\Lambda}B$ reaction. We find that our results are in agreement with previous calculations; the cross section is a smoothly decreasing function of the kaon polar angle for different combinations of particle-hole orbitals in the hypernucleus as well as for different kinematical conditions.

Contents

Chapter 1

Introduction

1.1 Hypernuclei

A hypernucleus is a nucleus where one or more of the nucleons have been replaced by a hyperon, i.e. a baryon containing one or more strange quarks. Thus, hypernuclei are part of the so-called "exotic" matter, having strangeness $S \neq 0$, and SU(3)-flavor symmetry is required in their theoretical treatment. The fact that hyperons have non-vanishing strangeness makes them unaffected by the Pauli exclusion principle: hyperons can thus penetrate deeply inside the nuclear system, providing a sensitive probe of the nuclear interior.

The most studied and well known hypernuclei are the ones containing the lightest hyperon, i.e. the Λ: their lifetime of about 10^{-11} to 10^{-10} s is long enough to give rise to sharp nuclear energy levels. The next lightest hyperon is the Σ, but the strong reaction $\Sigma N \rightarrow \Lambda N$ which takes place in nuclei makes Σ-hypernuclei unstable, and thus more difficult to study than Λ-hypernuclei. A variety of Λ-hypernuclei has been observed and studied experimentally: they can be seen in Fig. 1.1, where they are superimposed on the chart of regular nuclei.

Hypernuclear spectroscopy is an interesting field of study, since the presence of a hyperon can allow for the appearance of dynamical symmetries that are forbidden in ordinary nuclei by the Pauli principle. It is also an essential tool for the understanding of the hyperon-nucleon and hyperon-hyperon interaction, which is expected to play a crucial role in dense nuclear matter, such as the interior of neutron stars. For this reason, experimental data on hypernuclear properties have been collected since the mid 1950's using different reaction channels [1].

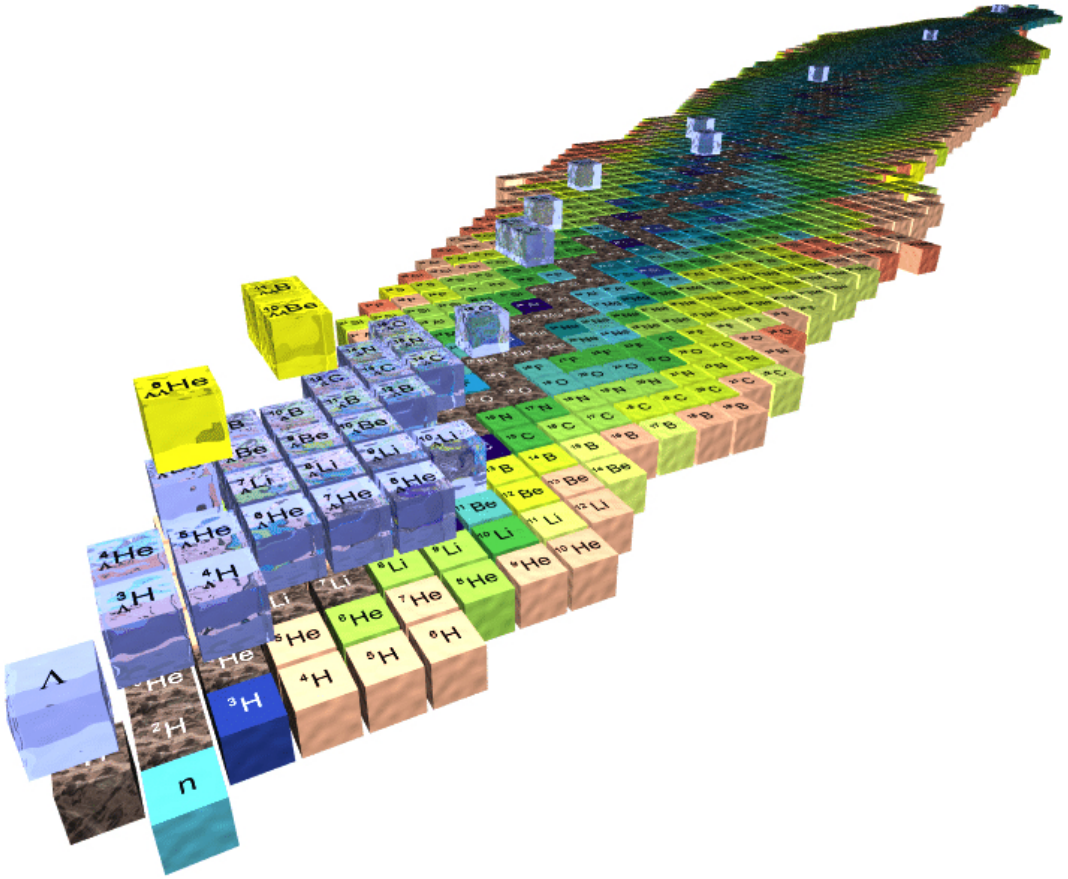

Figure 1.1: Nuclear chart including all the known nuclei and hypernuclei. The x axis corresponds to the number of neutrons, the y axis to the number of protons, and the z axis to the number of Λ hyperons. This image is from the "IX International Conference on Hypernuclear and Strange Particle Physics" at Johannes Gutenberg-Universität Mainz.

1.2 About this work

Currently, among the available reaction channels for the study of hypernuclear spectroscopy, the most promising one is $(e, e'K)$. Experimental studies of this reaction are currently being conducted or have been approved at Jefferson National Laboratory (JLab), Halls A and C; these include a variety of nuclear targets, such as ^{6}Li, ^{9}Be, ^{12}C, ^{16}O, ^{40}Ca or ^{48}Ca. It is clear from the experience on $(e, e'p)$ reactions that a sound theoretical background is needed to understand the experimental results, so this thesis aims at making a contribution to this knowledge.

In this work, thus, we will develop the theoretical framework that is necessary for the evaluation of differential cross sections of $(e, e'K)$ reactions: this includes the kinematics

of the nuclear reaction, as well as a model for its dynamics. We also develop a Python code to make numerical calculations of $(e, e'K)$ cross sections, and we test it on a ^{12}C target.

This thesis is structured as follows. In Chapter 2 we review the development and features of hypernuclear spectroscopy, and we go more in depth about the motivations of this field of study. In Chapter 3 we develop the formulae for triple differential cross sections of $(e, e'K)$ reactions in the impulse approximation, including a treatment of the leptonic and hadronic part of the reaction. Since a good knowledge of the elementary process $\gamma + p \to K + \Lambda$ is required in order to achieve a reasonable description of the nuclear reaction, in Chapter 4 we analyze the elementary process more in depth and we go over several models that can be employed to describe it. Then, in Chapter 5 we present our numerical calculations for the $^{12}C(e, e'K)^{12}_{\Lambda}B$ reaction and their results. Finally, Chapter 6 contains a few concluding remarks on our results, as well as possible future developments of this research.

Chapter 2

Overview of hypernuclear spectroscopy

2.1 Principles of hypernuclear spectroscopy

Λ hypernuclei can be produced through a variety of reactions with hadronic or electromagnetic beams. In the majority of these reactions, the hypernucleus is populated in a nucleon-hole, hyperon-particle excited state, since a nucleon in the target nucleus is converted to a Λ. Then, the hypernucleus decays through strong, electromagnetic and weak interactions, according to the nature of the state; the possible decays are schematically illustrated in Fig. 2.1. The Λ binding energies are usually higher than those for nucleons, and hypernuclei where the Λ is bound in an orbit above the p shell often decay by emitting nucleons. Widths of hypernuclear states are also narrower than those of ordinary nuclear states, since the ΛN interaction is weaker than the NN interaction, the ΛN spin-spin interaction is weak and no exchange term with nucleons is required. Thus, these widths are expected to be narrower than the spacing between the major shells, so hypernuclear states should be observable as reasonably narrow peaks. When hypernuclear states below particle emission threshold are populated, γ decays to the ground state take place; the ground state will, in turn, decay via weak interaction.

The first experiments conducted to study hypernuclei were emulsion experiments. Starting from the mid 1950's, the binding energies of light ($A \leq 16$) Λ hypernuclei were measured from weak decays, and it was found that the Λ potential depth was approximately 2/3 that of the nucleon. However, almost all of this data was limited to binding energies of ground states.

Hypernuclei are more conveniently studied via nuclear reactions. There are essentially

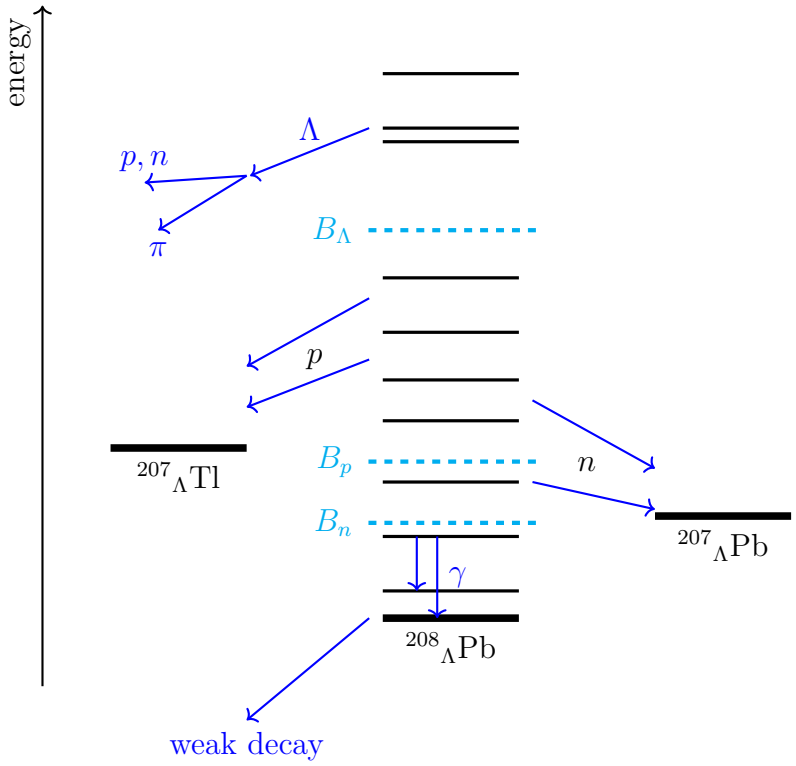

Figure 2.1: Hypernuclear states, exemplified for a $^{208}_{\Lambda}$Pb hypernucleus, with their decay modes. B_Λ, B_p and B_n denote the binding energies of a Λ, a proton and a neutron, respectively. This diagram is from [1].

two types of probes that can be used for this purpose: hadronic probes and electromagnetic probes.

At first (early 1970's), a lot of data on hypernuclei was collected from hadron-induced reactions. One is the strangeness exchange reaction

$$K^- + n \rightarrow \pi^- + \Lambda. \tag{2.1}$$

This reaction is characterized by a small momentum transfer $q \lesssim 200\,\mathrm{MeV/c}$, as it can be seen in Fig. 2.2, and a negligible spin-flip contribution at small pion angles (less than 10°), i.e. transitions with $\Delta l = \Delta s = 0$ dominate. The states that are mainly populated are substitutional states, where the nucleon is converted to a Λ in the same orbital. The spin-orbit splittings in p-shell hypernuclei were also found to be quite small. Moreover, because of the strong absorption of the kaon and pion, mainly the peripheral nucleons are involved in this reaction. This leads to a fairly high differential cross section (of the order of some mbarn/sr), but the missing mass spectra are not of very high quality, since the $\bar{u}$ quark in the K^- can annihilate with a valence quark in the neutron and form a three-quark resonance.

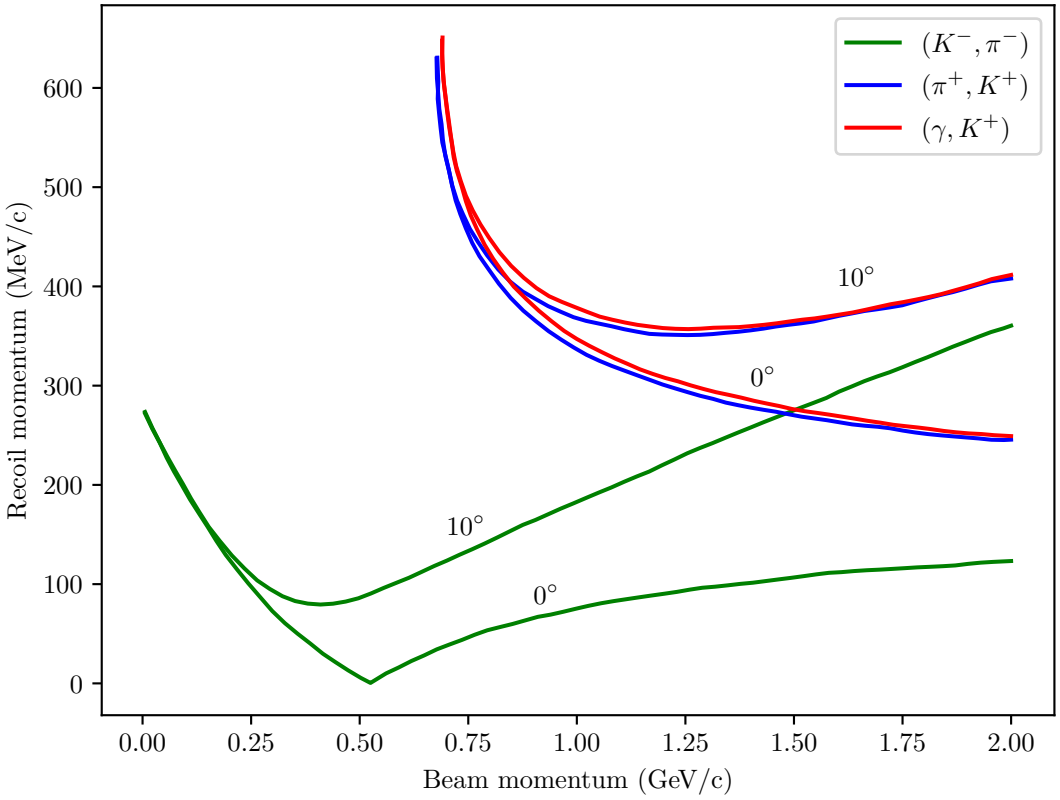

Figure 2.2: Recoil hypernucleus momentum dependence on the incident beam momentum for a ^{12}C target, plotted for kaon angles of 0° and 10°. This plot is from [1].

Another hadronic reaction that has been studied starting in the mid 1980's is the strangeness production

$$\pi^+ + n \rightarrow K^+ + \Lambda. \tag{2.2}$$

This has a higher momentum transfer with respect to the previous one, and the spin-flip contribution is slightly larger but still weak at small kaon angles. The larger momentum transfer makes it possible to excite high-spin hypernuclear states where the nucleon hole has a large angular momentum and the Λ has a small angular momentum. Transitions with $\Delta l = 1, 2$, $\Delta s = 0$ dominate, and the differential cross section is of order 10 μbarn/sr, which is smaller than the one for (K^-, π^-) reactions due to the higher momentum transfer. The data from this reaction on heavier nuclei have demonstrated the existence of deep lying shell model Λ orbitals in the nuclear medium, but the energy resolution is still not very good.

A more recent experimental technique is the study of gamma ray spectra of hyper-

nuclei, i.e. gamma ray hypernuclear spectroscopy. This is characterized by a very good energy resolution of a few keV; however, it only has access to hypernuclear states below nucleon emission threshold. Still, gamma ray hypernuclear spectroscopy is a powerful tool for the investigation of spin-dependent ΛN interactions, which requires very precise information on the level structure of hypernuclei: this makes it a complementary tool to reaction-based experiments.

An alternative reaction mechanism with a better energy and spatial resolution with respect to hadronic reactions is the electromagnetic production using a real or virtual photon:

$$\gamma + p \rightarrow K^+ + \Lambda. \tag{2.3}$$

The momentum transfer associated with this reaction is higher, $q \gtrsim 350\,\mathrm{MeV/c}$, which implies a smaller cross section, since the Λ has a smaller probability of sticking to the nuclear system. This reaction also has a strong spin-flip contribution, even at zero kaon angle, and transitions with $\Delta l = 2$, $\Delta s = 1$ dominate. The kaon distortion effects are quite small, ranging from approximately 10% to 50%. Moreover, the photon interacts relatively weakly with the nucleus, so the reaction is not confined to the nuclear surface, offering the possibility to study hypernuclear states with a deeply bound hyperon. Using electron beams, i.e. an electroproduction reaction that involves a virtual photon, allows for a resolution of several hundreds keV, which is better than hadron-induced reactions, but multiplet splitting is still problematic. However, electron spectroscopy makes it possible to explore more excited states than gamma ray spectroscopy, e.g. between nucleon and Λ emission threshold. In $(e, e'K)$ reactions the products are emitted at very forward angles, so it is necessary to detect the electron and the kaon in coincidence. There are several advantages, other than the aforementioned energy resolution, of studying electromagnetic production of hypernuclei, and particularly electroproduction, compared to hadron-induced reactions. First, the virtual photon can excite both natural and unnatural parity states with comparable strength, and makes it possible to obtain more information on the elementary process, since its mass and polarization can be varied independently. Also, electromagnetic production takes place on the proton, instead of the neutron in hadron-induced reactions: this allows to produce hypernuclei that are otherwise inaccessible, and opens the possibility to study charge dependent effects in mirror hypernuclei. Additionally, electron beams are very clean and under control, and can also be polarized, which is impossible for pions and kaons. Finally, from the theoretical point of view, the electromagnetic part of the reaction is very well understood from the very reliable field of QED.

For completeness, let us mention that there are five other possible electroproduction channels, namely

$$e + n \rightarrow e' + K^0 + \Lambda, \tag{2.4a}$$

$$e + p \rightarrow e' + K^+ + \Sigma^0, \tag{2.4b}$$

$$e + p \rightarrow e' + K^0 + \Sigma^+, \tag{2.4c}$$

$$e + n \rightarrow e' + K^+ + \Sigma^-, \tag{2.4d}$$

$$e + n \rightarrow e' + K^0 + \Sigma^0, \tag{2.4e}$$

but they are not the object of this work. One can also note that the cross section of Σ electroproduction will be different with respect to Λ electroproduction: this is because, due to isospin selectivity, only the N nucleon resonances can be exchanged for Λ production, while Δ's are also allowed in Σ production.

2.2 Motivations of hypernuclear spectroscopy

It is not straightforward to investigate the innermost part of a nucleus or deeply bound nuclear states using traditional experimental techniques. In fact, nucleon knockout reactions such as $(e, e'p)$ and $(p, 2p)$ can provide information on single-particle aspects of deeply bound states, but deeper states also become broader, thus prohibiting a precise spectroscopic investigation. The Λ particle that is present in hypernuclei provides an excellent probe, because it can penetrate deeply inside the nucleus being unaffected by the Pauli exclusion principle. This makes hypernuclear spectroscopy a very interesting tool in the study of nuclear systems.

Another reason for the interest in hypernuclear spectroscopy lies in the fact that it can provide valuable information on the hyperon production mechanism and the dynamics of the associated elementary process. The energy position of high-spin terms of Λ-spin doublets can be determined, as well as response functions (transition form factors) in a large momentum range.

Perhaps the most prominent motivation for the research in hypernuclear spectroscopy is the study of hyperon-nucleon (YN) and hyperon-hyperon (YY) interactions, in order to understand the role of strangeness in the context of hadronic interactions, and, in the end, achieve a unified description of baryon-baryon interactions. Severe difficulties were encountered in the determination of the YN potential from scattering data: hyperons

have relatively short lifetimes (of the order of 10^{-10} s) and suitable hyperon beams are not readily available; moreover, only the central part of these potential can be extracted from scattering experiments alone, leaving no information on the spin-dependent part. Due to this limitation, the knowledge in this field is still relatively incomplete (compared to nucleon-nucleon interactions), and hypernuclear spectroscopy has been seen as the alternative approach that could provide very important insights. What we know, e.g. in the ΛN case, is that this interaction is much weaker than the NN force: this is due to the fact that the Λ has zero isospin, so the exchange of a single vector meson, like the pion or the ρ, is forbidden, which leads to the absence of a dominant tensor force. However, some of the most outstanding issues in this field are the isospin dependence and the role of three-body forces in YN interactions.

Hypernuclei also offer the possibility to study mesonic ($\Lambda \to N + \pi$) and non-mesonic ($Y + N \to N + N$) weak decays in the nuclear medium. The last one, in particular, is a unique opportunity to study the strangeness-changing weak decay, so that the four-fermion weak vertex may be investigated.

Additionally, hypernuclear spectroscopy can be a useful tool for the study of baryon resonances. Our current theoretical understanding of baryon (and, more specifically, nucleon) excitation spectra comes from the quark model framework; this model, however, predicts a much richer spectrum than what has been observed in $\pi N \to \pi N$ scattering experiments, and there are a number of so-called "missing resonances". These could be identified through the study of the electromagnetic production of hypernuclei, since nucleon resonances are exchanged in the reaction. This can also provide an opportunity to study the coupling of N^* and Δ resonances to meson-hyperon final states, and compare it to the SU(3) predictions.

Another very interesting motivation for studying hypernuclei is their relevance in neutron stars. A free Λ is unstable, and will primarily decay into a pion and a nucleon via the weak interaction; however, in a stellar environment it will interact strongly with other nucleons, forming a hypernucleus. The appearance of hyperons is thus expected to be energetically favored in dense nuclear matter. Many models that predict the presence of hyperons in neutron star cores rule out the existence of two-solar-mass neutron stars, which have instead been recently observed. This suggests that our knowledge of nuclear interactions involving hyperons and hyperon matter is incomplete, and is known as the "hyperon puzzle". In the light of this, studying electroproduction reactions on heavy nuclear targets with large neutron excess, such as ^{208}Pb, could provide our best proxy for the neutron star environment [2].

Interactions including hyperons are also pertinent in the field of heavy-ion collisions, which is mainly concerned with the analysis of the nuclear equation of state, the possible phase transitions from hadronic matter to quark-gluon plasma and the modification of hadron properties in dense, strong-interacting environments (e.g. the magnetic moment of the Λ in the nuclear environment). The precise measurement of single-particle level positions of the Λ from ${}^{12}_{\Lambda}\mathrm{C}$ to ${}^{208}_{\Lambda}\mathrm{Pb}$ can shed some light on the quark deconfinement reaction in the nuclear medium.

2.3 Tools for the theoretical study of hypernucleus electroproduction

Let us conclude this chapter by introducing the tools that are needed to conduct a theoretical analysis of electroproduction of hypernuclei. The leptonic part of the reaction is well understood from QED, so the main difficulties arise from the hadronic part.

The first ingredient that is needed is the state of the target nucleus and the produced hypernucleus, i.e. their wavefunctions. If one considers the reaction to take place on the full nucleus and hypernucleus, then the full nuclear and hypernuclear wavefunctions are needed, and obtaining them becomes increasingly difficult as the size of the nucleus increases. Alternatively, on can adopt a factorization approach, where the virtual photon is considered to interact with a single nucleon: this is a good approximation when the photon momentum is high enough. In this case, one only needs the wavefunctions of the bound nucleon and hyperon, which can be obtained from mean field methods or ab initio methods.

Then, one needs the distorted wavefunction of the kaon, which can be obtained from the study of the hypernucleus' optical potential. However, since the kaon distortion is rather small, we will neglect it in this work.

The last ingredient is the amplitude for the elementary reaction $\gamma + p \to K^+ + \Lambda$. There are two main approaches to tackle it: QCD or effective field theories (quantum hadrodynamics). The parton-based QCD approach uses quark and gluon degrees of freedom, and the strange quarks that appear in the final state emerge from the quark sea. In these models, hadronic resonances are implicitly included as excited states, making the number of free parameters relatively small. The internal structure of hadrons is also implicitly included, and doesn't need to be modeled phenomenologically. However, using

quark models for electroproduction of hypernuclei is extremely complicated, and below the energies where QCD can be treated perturbatively quarks are not the ideal degrees of freedom to use. Effective field theories, on the other hand, use mesons and baryons as degrees of freedom, and the elementary reaction is modeled as the exchange of baryon and meson resonances, each one with its own properties. This makes the number of free parameters of the theory rather large; these free parameters are generally fitted to photoproduction data, and since the χ^2 hypersurface doesn't have a pronounced global minimum, but rather many local minima, one can have many different sets of parameters that describe photoproduction equally well but give different results when extended to electroproduction. There are several types of hadrodynamical approaches, which include isobar models, Regge and Regge-plus-resonance models and multipole approaches; in this work we will use an isobar model, since it is the one that can be integrated in the full nuclear reaction in the most straightforward way.

Chapter 3

Formalism

In this section we are going to address the formalism that is necessary to tackle the hypernucleus electroproduction reaction and its cross section. The following conventions will be used throughout this thesis: natural units $\hbar = c = 1$, and the $(+,-,-,-)$ Minkowski metric, i.e. $g^{\mu\nu} = \mathrm{diag}(1,-1,-1,-1)$.

3.1 General cross section formula

Our goal is to evaluate the differential cross section for kaon electroproduction on nuclei. We write the reaction in the following way:

$$e(k) + A(P) \rightarrow e'(k') + K^+(p'_1) + {}_\Lambda A(P') \tag{3.1}$$

where the four-momenta of the particles are indicated inside the brackets (we are following the notation of [3]). The components of these four-momenta are denoted as follows: $k^\mu = (E_k, \mathbf{k})$, $P^\mu = (E_P, \mathbf{P})$, $k'^\mu = (E_{k'}, \mathbf{k}')$, $p_1'^\mu = (E_{p'_1}, \mathbf{p}'_1)$, $P'^\mu = (E_{P'}, \mathbf{P}')$. We also define the momentum transfer $q^\mu = k^\mu - k'^\mu = (\omega, \mathbf{q})$, which corresponds to the four-momentum of the virtual photon. In our case q^μ is space-like ($q^2 = q_\mu q^\mu < 0$), so we define the photon virtuality $Q^2 = -q^2 = |\mathbf{q}|^2 - \omega^2$.

We will consider the above reaction in the impulse approximation regime, where the wavelength of the exchanged photon is smaller than the typical internuclear distance of 1.5 fm. This corresponds to an energy greater than about 130 MeV, which means that we can assume the electron to be in an ultra-relativistic regime: in the upcoming calculations we will therefore use $|\mathbf{k}| \simeq E_k$, $|\mathbf{k}'| \simeq E_{k'}$.

The cross section for a generic $2 \to 3$ particle reaction can be written as (see e.g. Eq. 5.22 of [8])

$$d\sigma = \frac{(2\pi)^4 \delta^4(k + P - k' - p_1' - P')}{(2E_k)\,|\mathbf{v}_k - \mathbf{v}_A|} |\mathcal{M}|^2 \frac{d^3\mathbf{k}'}{2E_{k'}(2\pi)^3} \frac{d^3\mathbf{p_1'}}{2E_{p_1'}(2\pi)^3} \frac{d^3\mathbf{P}'}{(2\pi)^3} \tag{3.2}$$

where $\mathbf{v}_k - \mathbf{v}_A$ is the relative velocity of the electron with respect to the target nucleus. Note that, in the above formula, we have included the normalization factor $\frac{1}{2E}$ for the electrons and kaon, but not for the nucleus and hypernucleus: this is because for the electrons and kaon we will adopt the normalization for free spinors $u_p^\dagger u_p = 2p^0$, while for the nucleus and hypernucleus we will adopt the normalization for bound spinors $\int d^3p\, u_p^\dagger u_p = 1$.

We will simplify Eq. (3.2) in the laboratory frame of reference (see Fig. 3.1), where $P^\mu = (M_A, \mathbf{0})$, with M_A being the mass of the target nucleus, and where we take the z axis in the direction of $\mathbf{q}$. The leptonic plane contains $\mathbf{k}$, $\mathbf{k}'$ and $\mathbf{q}$: we will identify it with the xz plane. The electron scattering angle is θ', and the direction of the incident electron with respect to the z axis is denoted by the angle α. The hadronic plane contains $\mathbf{q}$, $\mathbf{p_1'}$ and $\mathbf{P}'$, and the kaon scattering angle is denoted by θ_1'; the angle this plane forms with respect to the leptonic plane will be called ϕ_1'.

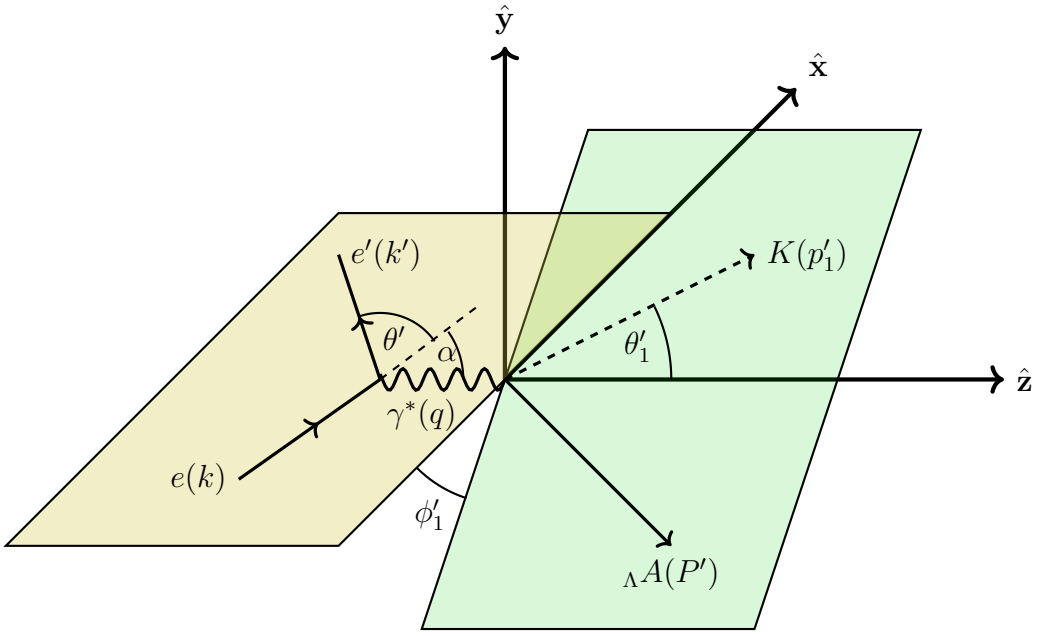

Figure 3.1: Laboratory frame of reference, with the leptonic plane in yellow and the hadronic plane in green.

We can start by using the spatial part of the delta function to integrate out the three-momentum of the recoiling hypernucleus and by noting that in the ultra-relativistic

regime $\mathbf{v}_k - \mathbf{v}_A = c = 1$. This leads to

$$d\sigma = \frac{\delta(E_k + M_A - E_{k'} - E_{p'_1} - E_{P'})}{2^3(2\pi)^5 E_k E_{k'} E_{p'_1}}\, d^3\mathbf{k}'\, d^3\mathbf{p}'_\mathbf{1}\, |\mathcal{M}|^2. \tag{3.3}$$

The two differentials can be rewritten in spherical coordinates: if we define $\Omega'_1 = (\theta'_1, \phi'_1)$, then

$$d^3\mathbf{k}' = 2\pi E_{k'}^2\, dE_{k'} d(\cos\theta') \tag{3.4a}$$

$$d^3\mathbf{p}'_\mathbf{1} = p_1'^2\, dp'_1 d\Omega'_1 = p'_1 E_{p'_1}\, dE_{p'_1} d\Omega'_1 = \sqrt{E_{p'_1}^2 - m_K^2 - -} E_{p'_1}\, dE_{p'_1} d\Omega'_1. \tag{3.4b}$$

The second equality is obtained by using $p'_1 dp'_1 = E_{p'_1} dE_{p'_1}$, which comes directly from the differentiation of the mass-shell condition $E_{p'_1}^2 = p_1'^2 + m_K^2$.
Inserting the differentials (3.4) into Eq. (3.3) we get

$$\frac{d^3\sigma}{dE_{k'} d(\cos\theta') d\Omega'_1} = \frac{\delta(E_k + M_A - E_{k'} - E_{p'_1} - E_{P'})}{2^3(2\pi)^4 E_k} E_{k'} \sqrt{E_{p'_1}^2 - m_K^2}\, |\mathcal{M}|^2\, dE_{p'_1}. \tag{3.5}$$

A more explicit expression for the energy of the recoiling hypernucleus is given by

$$\begin{aligned} E_{P'} &= \sqrt{|\mathbf{P}'|^2 + M_{_{\Lambda A}}^2} = \\ &= \sqrt{|\mathbf{q} - \mathbf{p}'_1|^2 + \left[M_A - \left(m_p - E_B^{(p)}\right) + \left(m_\Lambda - E_B^{(\Lambda)}\right)\right]^2} = \\ &= \sqrt{|\mathbf{q}|^2 + E_{p'_1}^2 - m_K^2 - 2|\mathbf{q}|\sqrt{E_{p'_1}^2 - m_K^2}\cos\theta'_1 + \left[M_A - \left(m_p - E_B^{(p)}\right) + \left(m_\Lambda - E_B^{(\Lambda)}\right)\right]^2}, \end{aligned} \tag{3.6}$$

where $|\mathbf{q}| = \sqrt{E_k^2 + E_{k'}^2 - 2E_k E_{k'}\cos\theta'}$, and $E_B^{(p)}$ and $E_B^{(\Lambda)}$ are the binding energies of a proton and of a Λ, respectively.
We can now use the remaining delta function to integrate out $E_{p'_1}$: defining $f(E_{p'_1}) = E_k + M_A - E_{k'} - E_{p'_1} - E_{P'}(E_{p'_1})$, then

$$\delta\left(f(E_{p'_1})\right) = \frac{\delta(E_{p'_1} - E^*_{p'_1})}{|f'(E^*_{p'_1})|}, \tag{3.7}$$

where $E^*_{p'_1}$ is the root of the equation $f(E_{p'_1}) = 0$. The triple differential cross section now takes the form

$$\frac{d^3\sigma}{dE_{k'} d(\cos\theta') d\Omega'_1} = \frac{E_{k'}\sqrt{E_{p'_1}^{*2} - m_K^2}}{2^3(2\pi)^4 E_k |f'(E^*_{p'_1})|} |\mathcal{M}|^2. \tag{3.8}$$

More explicitly, $f'(E_{p'_1})$ is given by

$$f'(E_{p'_1}) = -1 - \frac{E_{p'_1}\left(1 - |\mathbf{q}|\cos\theta'_1 \Big/ \sqrt{E_{p'_1}^2 - m_K^2}\right)}{\sqrt{|\mathbf{q}|^2 + E_{p'_1}^2 - m_K^2 - 2|\mathbf{q}|\sqrt{E_{p'_1}^2 - m_K^2}\cos\theta'_1 + M_{_{\Lambda A}}^2}}. \tag{3.9}$$

To conclude this section, let us also compute the analytical expression for $E^*_{p'_1}$. Setting $f(E_{p'_1}) = 0$ and inserting expression (3.6) for $E_{P'}$ we get

$$E_k + M_A - E_{k'} - E_{p'_1} = \sqrt{|\mathbf{q}|^2 + E^2_{p'_1} - m^2_K - 2|\mathbf{q}|\sqrt{E^2_{p'_1} - m^2_K}\cos\theta'_1 + M^2_{{}_\Lambda A}}. \quad (3.10)$$

Since E_k, M_A and $E_{k'}$ do not depend on $E_{p'_1}$, we can collect them under the name of $C \equiv E_k + M_A - E_{k'}$. Using this shorthand notation and squaring both terms of the above equation, we obtain

$$\begin{cases} -C^2 + 2CE_{p'_1} + |\mathbf{q}|^2 - m^2_K + M^2_{{}_\Lambda A} = 2|\mathbf{q}|\sqrt{E^2_{p'_1} - m^2_K}\cos\theta'_1 \\ E_{p'_1} \leq C. \end{cases} \quad (3.11)$$

The condition in the second line comes from requiring the positivity of the left-hand side of Eq.(3.10), and has the clear physical meaning that the energy of the outgoing kaon should not exceed the energy of the incoming electron plus the nucleus mass minus the energy of the outgoing electron. After introducing another shorthand notation $D \equiv -C^2 + |\mathbf{q}|^2 - m^2_K + M^2_{{}_\Lambda A}$ and squaring both sides of the above equation, we are left with

$$\begin{cases} \left(C^2 - |\mathbf{q}|^2\cos^2\theta'_1\right) E^2_{p'_1} + CDE_{p'_1} + \dfrac{D^2}{4} + |\mathbf{q}|^2 m^2_K \cos^2\theta'_1 = 0 \\ \dfrac{D + 2CE_{p'_1}}{\cos\theta'_1} \geq 0 \\ E_{p'_1} \leq C. \end{cases} \quad (3.12)$$

The solution for the second-degree equation on the first line is

$$E^*_{p'_1} = \frac{-CD \pm \sqrt{C^2D^2 - \left(C^2 - |\mathbf{q}|^2\cos^2\theta'_1\right)\left(D^2 + 4|\mathbf{q}|^2 m^2_K \cos^2\theta'_1\right)}}{2\left(C^2 - |\mathbf{q}|^2\cos^2\theta'_1\right)}. \quad (3.13)$$

3.2 Factorization of the matrix element

Having completely treated the kinematics of the reaction, we now turn to the matrix element $\mathcal{M}$. In the impulse approximation (see Fig. 3.2), only one virtual photon is exchanged, so using standard Feynman rules the matrix element can be written as

$$\mathcal{M} = \bar{u}_f \gamma_\mu u_i \frac{e^2}{q^2} \left\langle K^+ {}_\Lambda A \right| J^\mu(q) \left| A \right\rangle, \quad (3.14)$$

where $u_i = u(\mathbf{k}, h)$ and $\bar{u}_f = \bar{u}(\mathbf{k}', h')$ are the spinors for the incoming and outgoing electron, respectively, which depend on the corresponding electron helicities h and h',

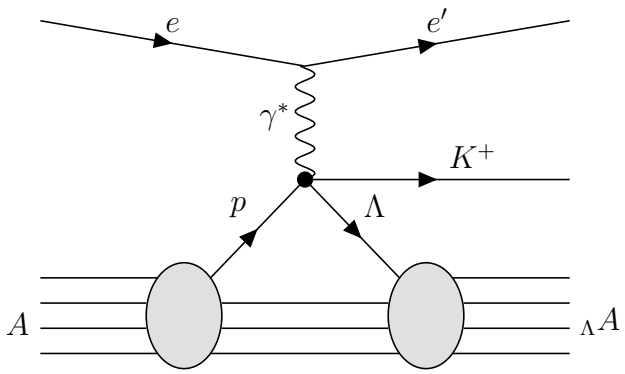

Figure 3.2: Feynman diagram for the $e + A \to e' + K^+ + {}_\Lambda A$ process in the impulse approximation: the virtual photon interacts with a single proton from the target nucleus, and the other nucleons act as spectators.

and are normalized as $u^\dagger(p)u(p) = 2p^0$, $\bar{u}(p)u(p) = 2m$; $|A\rangle$ and $|K^+{}_\Lambda A\rangle$ are the initial and final hadronic states, and J^μ is the hadronic current operator.

The modulus squared of the matrix element can then be cast in the form

$$|\mathcal{M}|^2 = \left(\frac{e^2}{q^2}\right)^2 L_{\mu\nu} W^{\mu\nu} \tag{3.15}$$

where $L_{\mu\nu}$ and $W^{\mu\nu}$ are the leptonic and hadronic tensor, respectively, and are defined as

$$L_{\mu\nu} = \bar{u}_f \gamma_\mu u_i \bar{u}_i \gamma_\nu u_f = tr\left(u_f \bar{u}_f \gamma_\mu u_i \bar{u}_i \gamma_\nu\right) \tag{3.16}$$

$$W^{\mu\nu} = \sum_{\alpha_A, \alpha_Y} \left\langle K^+{}_\Lambda A \right| J^\mu(q) \left|A\right\rangle_{\alpha_A, \alpha_Y} \left\langle K^+{}_\Lambda A \right| J^\nu(q) \left|A\right\rangle^*_{\alpha_A, \alpha_Y} \tag{3.17}$$

where α_A and α_Y are the quantum numbers that define the transition from the nucleus to the hypernucleus.

Let us now see a consideration that will allow us to simplify the sum over repeated indices in Eq. (3.15). For convenience, let us define

$$l_\mu \equiv \bar{u}_f \gamma_\mu u_i \quad \text{and} \quad w^\mu_{\alpha_A, \alpha_Y} \equiv \left\langle K^+{}_\Lambda A \right| J^\mu(q) \left|A\right\rangle_{\alpha_A, \alpha_Y}, \tag{3.18}$$

so that

$$L_{\mu\nu} = l_\mu l^*_\nu \quad \text{and} \quad W^{\mu\nu} = \sum_{\alpha_A, \alpha_Y} w^\mu_{\alpha_A, \alpha_Y} w^{*\nu}_{\alpha_A, \alpha_Y}. \tag{3.19}$$

Gauge invariance, or equivalently lepton current conservation, implies

$$q^\mu l_\mu = 0 \Rightarrow \omega l^0 - |\mathbf{q}| l^3 = 0 \Rightarrow l^0 = \frac{|\mathbf{q}|}{\omega} l^3. \tag{3.20}$$

Similarly, hadron current conservation implies (omitting the quantum numbers for brevity)

$$w^0 = \frac{|\mathbf{q}|}{\omega} w^3. \tag{3.21}$$

Consequently,

$$\begin{aligned} l_\mu w^\mu &= \frac{|\mathbf{q}|^2}{\omega^2} l^3 w^3 - l^1 w^1 - l^2 w^2 - l^3 w^3 = -l^1 w^1 - l^2 w^2 - \frac{\omega^2 - |\mathbf{q}|^2}{\omega^2} l^3 w^3 \\ &= -l^1 w^1 - l^2 w^2 - \frac{q^2}{\omega^2} l^3 w^3 = l_i w^i \left(\frac{-Q^2}{\omega^2} \right)^{\delta_{i3}}, \end{aligned} \tag{3.22}$$

where $i = 1, 2, 3$. This means that we can restrict ourselves to the space-like parts of the leptonic and hadronic tensors, provided that we include a factor $\frac{-Q^2}{\omega^2}$ for each third component. It is convenient to include this factor in the leptonic tensor and ignore it in the hadronic one: we can thus define a modified leptonic tensor

$$\tilde{L}_{ij} \equiv \left(\frac{-Q^2}{\omega^2} \right)^{\delta_{i3}+\delta_{j3}} L_{ij}, \tag{3.23}$$

and Eq. (3.15) becomes

$$|\mathcal{M}|^2 = \left(\frac{e^2}{q^2} \right)^2 \tilde{L}_{ij} W^{ij}. \tag{3.24}$$

3.3 The leptonic tensor

3.3.1 Expansion for the four possible polarization combinations

Let us compute the leptonic tensor in four different cases, corresponding to the four combinations of polarized/unpolarized incoming/outgoing electron beams. When a beam is unpolarized, in the leptonic tensor we will take the sum over the two possible helicities, and we will use the identity

$$\sum_{h=\pm 1} u(p,h)\bar{u}(p,h) = \not{p}, \tag{3.25}$$

where we have neglected the mass because the electron is in the ultra-relativistic regime. On the other hand, when a beam is polarized, we will project the desired helicity by first summing over the possible helicities and then acting on the sum with the projection operator

$$P_h = \frac{1 + h\gamma^5}{2}. \tag{3.26}$$

It is now easy to compute the four possible leptonic tensors following this procedure and using trace identities for the Dirac matrices (see Appendix A.2). When both the

incoming and outgoing beams are unpolarized, the leptonic tensor reads

$$\begin{aligned} L^{(0)}_{\mu\nu} &= tr\left[\sum_{h,h'} u(k',h')\bar{u}(k',h')\gamma_\mu u(k,h)\bar{u}(k,h)\gamma_\nu\right] \\ &= tr(\not{k}'\gamma_\mu \not{k}\gamma_\nu) \\ &= 4(k_\mu k'_\nu + k'_\mu k_\nu - k\cdot k' g_{\mu\nu}) \end{aligned} \tag{3.27}$$

(to obtain the third line from the second one we have used Eq. (A.7)).

When the incoming beam is polarized and the outgoing beam is unpolarized, the result is

$$\begin{aligned} L^{(1)}_{\mu\nu} &= tr\left[\left(\frac{1+h\gamma^5}{2}\right)\sum_{h,h'} u(k',h')\bar{u}(k',h')\gamma_\mu u(k,h)\bar{u}(k,h)\gamma_\nu\right] \\ &= \frac{1}{2}tr[(1+h\gamma^5)(\not{k}'\gamma_\mu \not{k}\gamma_\nu)] \\ &= \frac{1}{2}L^{(0)}_{\mu\nu} + \frac{h}{2}k'^\alpha k^\beta(-4i\epsilon_{\alpha\mu\beta\nu}) \\ &= 2(k_\mu k'_\nu + k'_\mu k_\nu - k\cdot k' g_{\mu\nu} - ihk^\alpha k'^\beta \epsilon_{\mu\nu\alpha\beta}), \end{aligned} \tag{3.28}$$

where $\epsilon_{\mu\nu\alpha\beta}$ is the anti-symmetric tensor with $\epsilon_{0123} = 1$ (to go from the second to the third line we have used Eq. (A.10)).

Similarly, when the incoming beam is unpolarized and the outgoing beam is polarized we have

$$L^{(2)}_{\mu\nu} = 2(k_\mu k'_\nu + k'_\mu k_\nu - k\cdot k' g_{\mu\nu} - ih'k^\alpha k'^\beta \epsilon_{\mu\nu\alpha\beta}). \tag{3.29}$$

Finally, when both the incoming and outgoing beams are polarized, the leptonic tensor becomes

$$\begin{aligned} L^{(3)}_{\mu\nu} &= tr\left[\left(\frac{1+h\gamma^5}{2}\right)\left(\frac{1+h'\gamma^5}{2}\right)\sum_{h,h'} u(k',h')\bar{u}(k',h')\gamma_\mu u(k,h)\bar{u}(k,h)\gamma_\nu\right] \\ &= \frac{1}{4}tr[(1+h\gamma^5)(1+h'\gamma^5)(\not{k}'\gamma_\mu \not{k}\gamma_\nu)] \\ &= \frac{1}{4}L^{(0)}_{\mu\nu} + \frac{h+h'}{4}k'^\alpha k^\beta(-4i\epsilon_{\alpha\mu\beta\nu}) + \frac{hh'}{4}L^{(0)}_{\mu\nu} \\ &= (1+hh')(k_\mu k'_\nu + k'_\mu k_\nu - k\cdot k' g_{\mu\nu}) - i(h+h')k^\alpha k'^\beta \epsilon_{\mu\nu\alpha\beta} \end{aligned} \tag{3.30}$$

(for the last term of the third line we have used Eq. (A.3)).

3.3.2 Components of the fully unpolarized leptonic tensor

It is now our goal to compute the space-like components of the modified leptonic tensor in the fully unpolarized case more explicitly. First, it is customary to define the virtual

photon polarization density matrix as

$$\rho_{ij} = \frac{1}{4Q^2}\tilde{L}_{ij}, \tag{3.31}$$

which, for the fully unpolarized case, becomes

$$\rho_{ij} = \frac{1}{Q^2}\left(\frac{-Q^2}{\omega^2}\right)^{\delta_{i3}+\delta_{j3}}(k_i k'_j + k'_i k_j + k\cdot k'\delta_{ij}). \tag{3.32}$$

Let us also define the transverse and longitudinal polarization parameters, respectively, as

$$\epsilon = \frac{\rho_{11}-\rho_{22}}{\rho_{11}+\rho_{22}}, \qquad \epsilon_L = \frac{\rho_{33}}{\rho_{11}+\rho_{22}}. \tag{3.33}$$

We are now going to calculate the components of ρ in the laboratory frame. Let us recall that the components of $\mathbf{k}$, $\mathbf{k}'$ and $\mathbf{q}$ in this frame are:

$$\mathbf{k} = (k_1, 0, k_3) \tag{3.34a}$$

$$\mathbf{k}' = (k'_1, 0, k'_3) \tag{3.34b}$$

$$\mathbf{q} = (0, 0, |\mathbf{q}|) \tag{3.34c}$$

The fact that $\mathbf{q} = \mathbf{k} - \mathbf{k}'$ implies that $k_1 = k'_1$ and $k_3 - k'_3 = |\mathbf{q}|$. We can also evaluate the x and z components of $\mathbf{k}$ and $\mathbf{k}'$ by considering the following scalar and vector products:

$$(\mathbf{k}\times\mathbf{k}')_2 = |\mathbf{k}||\mathbf{k}'|\sin\theta' = (k_3k'_1 - k'_3k_1) = k_1|\mathbf{q}| \quad \Rightarrow k_1 = k'_1 = \frac{E_kE_{k'}\sin\theta'}{|\mathbf{q}|} \tag{3.35a}$$

$$\mathbf{k}\cdot\mathbf{q} = |\mathbf{k}|^2 - |\mathbf{k}||\mathbf{k}'|\cos\theta' = k_3|\mathbf{q}| \quad \Rightarrow k_3 = \frac{E_k}{|\mathbf{q}|}(E_k - E_{k'}\cos\theta') \tag{3.35b}$$

$$\mathbf{k}'\cdot\mathbf{q} = |\mathbf{k}||\mathbf{k}'|\cos\theta' - |\mathbf{k}'|^2 = k'_3|\mathbf{q}| \quad \Rightarrow k'_3 = \frac{E_{k'}}{|\mathbf{q}|}(E_k\cos\theta' - E_{k'}) \tag{3.35c}$$

In view the upcoming computations, it is useful to evaluate the following quantities, too:

$$Q^2 = -(k-k')^2 = 2k\cdot k' = 2(E_kE_{k'} - E_kE_{k'}\cos\theta') = 4E_kE_{k'}\sin^2\frac{\theta'}{2}, \tag{3.36}$$

$$\begin{aligned} E_k + E_{k'} &= \sqrt{(E_k+E_{k'})^2} = \sqrt{[(E_k+E_{k'})^2 - |\mathbf{k}-\mathbf{k}'|^2] + |\mathbf{q}|^2} = \\ &= \sqrt{[2E_kE_{k'} + 2E_kE_{k'}\cos\theta'] + |\mathbf{q}|^2} = \sqrt{4E_kE_{k'}\cos^2\frac{\theta'}{2} + |\mathbf{q}|^2}. \end{aligned} \tag{3.37}$$

We are now ready to insert the components of Eq.ns (3.35) into Eq. (3.32). Starting with the 11 and 22 components, we have

$$\rho_{11} = \frac{1}{Q^2}\left(2\frac{E_k^2E_{k'}^2\sin^2\theta'}{|\mathbf{q}|^2} + \frac{Q^2}{2}\right) = \frac{1}{Q^2}\left(2\frac{Q^4\cdot 4\sin^2\frac{\theta'}{2}\cos^2\frac{\theta'}{2}}{16\sin^4\frac{\theta'}{2}\cdot|\mathbf{q}|^2} + \frac{Q^2}{2}\right) = \frac{Q^2}{2|\mathbf{q}|^2}\cot^2\frac{\theta'}{2} + \frac{1}{2} \tag{3.38}$$

$$\rho_{22} = \frac{1}{Q^2} \cdot \frac{Q^2}{2} = \frac{1}{2}. \tag{3.39}$$

This allows us to compute

$$\epsilon = \frac{\frac{Q^2}{2|\mathbf{q}|^2}\cot^2\frac{\theta'}{2}}{\frac{Q^2}{2|\mathbf{q}|^2}\cot^2\frac{\theta'}{2}+1} = \left(1 + 2\frac{|\mathbf{q}|^2}{Q^2}\tan^2\frac{\theta'}{2}\right)^{-1}. \tag{3.40}$$

It is useful to solve this equation for the recurring combination $\frac{Q^2}{2|\mathbf{q}|^2}\cot^2\frac{\theta'}{2}$: the result is

$$\frac{Q^2}{2|\mathbf{q}|^2}\cot^2\frac{\theta'}{2} = \frac{\epsilon}{1-\epsilon}. \tag{3.41}$$

We can also rewrite ρ_{11} in terms of ϵ:

$$\rho_{11} = \frac{\epsilon}{1-\epsilon} + \frac{1}{2} = \frac{1}{2}\frac{1+\epsilon}{1-\epsilon}. \tag{3.42}$$

Turning to the calculation of ρ_{33}, we have

$$\begin{aligned}
\rho_{33} &= \frac{Q^2}{\omega^4}\left[2\frac{E_k E_{k'}}{|\mathbf{q}|^2}(E_k - E_{k'}\cos\theta')(E_k\cos\theta' - E_{k'}) + \frac{Q^2}{2}\right] = \\
&= \frac{Q^2}{\omega^4}\left[\frac{Q^2}{2\sin^2\frac{\theta'}{2}|\mathbf{q}|^2}(E_k^2\cos\theta' + E_{k'}^2\cos\theta' - E_k E_{k'} - E_k E_{k'}\cos^2\theta' \pm 2E_k E_{k'}\cos\theta') + \frac{Q^2}{2}\right] = \\
&= \frac{Q^4}{\omega^4}\left[\frac{1}{2\sin^2\frac{\theta'}{2}|\mathbf{q}|^2}((E_k - E_{k'})^2\cos\theta' - E_k E_{k'}(1-\cos\theta')^2) + \frac{1}{2}\right] = \\
&= \frac{Q^4}{\omega^4}\left[\frac{1}{2\sin^2\frac{\theta'}{2}|\mathbf{q}|^2}\left(\omega^2\cos\theta' - \frac{Q^2}{4\sin^2\theta'}4\sin^4\theta'\right) + \frac{1}{2}\right] = \\
&= \frac{Q^4}{\omega^4}\left[\frac{\omega^2(1-2\sin^2\frac{\theta'}{2})}{2\sin^2\frac{\theta'}{2}|\mathbf{q}|^2} - \frac{Q^2}{2|\mathbf{q}|^2} + \frac{1}{2}\right] = \frac{Q^4}{\omega^4}\left[\frac{\omega^2}{2\sin^2\frac{\theta'}{2}|\mathbf{q}|^2} - \frac{\omega^2}{|\mathbf{q}|^2} + \frac{\omega^2}{2|\mathbf{q}|^2}\right] = \\
&= \frac{Q^4}{\omega^2}\frac{1-\sin^2\frac{\theta'}{2}}{2\sin^2\frac{\theta'}{2}|\mathbf{q}|^2} = \frac{Q^4}{\omega^2}\frac{\cot^2\frac{\theta'}{2}}{2|\mathbf{q}|^2} = \frac{Q^2}{\omega^2}\frac{Q^2}{2|\mathbf{q}|^2}\cot^2\frac{\theta'}{2} = \frac{Q^2}{\omega^2}\frac{\epsilon}{1-\epsilon}
\end{aligned} \tag{3.43}$$

where, in the second line, $\pm 2E_k E_{k'}\cos\theta'$ means that we are adding and subtracting this term. Thus,

$$\epsilon_L = \frac{Q^2}{\omega^2}\frac{\epsilon}{1-\epsilon} \cdot \left(\frac{1}{2}\frac{1+\epsilon}{1-\epsilon} + \frac{1}{2}\right)^{-1} = \frac{Q^2}{\omega^2}\epsilon. \tag{3.44}$$

The last non-vanishing component of ρ_{ij} is

$$\begin{aligned}
\rho_{13} = \rho_{31} &= -\frac{1}{\omega^2}\frac{E_k E_{k'}\sin\theta'}{|\mathbf{q}|}\left[\frac{E_k}{|\mathbf{q}|}(E_k - E_{k'}\cos\theta') + \frac{E_{k'}}{|\mathbf{q}|}(E_k\cos\theta' - E_{k'})\right] = \\
&= -\frac{Q^2\sin\theta'}{4\sin^2\frac{\theta'}{2}|\mathbf{q}|^2}\frac{E_k^2 - E_{k'}^2}{\omega^2}.
\end{aligned} \tag{3.45}$$

Let us compute the two fractions separately for the sake of clarity:

$$-\frac{Q^2\sin\theta'}{4\sin^2\frac{\theta'}{2}|\mathbf{q}|^2}=-\frac{2Q^2\sin\frac{\theta'}{2}\cos\frac{\theta'}{2}}{4\sin^2\frac{\theta'}{2}|\mathbf{q}|^2}=-\frac{Q^2\cot\frac{\theta'}{2}}{2|\mathbf{q}|^2}=-\frac{Q}{|\mathbf{q}|}\sqrt{\frac{\epsilon}{2(1-\epsilon)}}, \tag{3.46}$$

$$\frac{E_k^2-E_{k'}^2}{\omega^2}=\frac{E_k+E_{k'}}{\omega}=\frac{\sqrt{4E_kE_{k'}\cos^2\frac{\theta'}{2}+|\mathbf{q}|^2}}{\omega}=\frac{|\mathbf{q}|}{\omega}\sqrt{\frac{Q^2\cos^2\frac{\theta'}{2}}{\sin^2\frac{\theta'}{2}|\mathbf{q}|^2}+1}=\frac{|\mathbf{q}|}{\omega}\sqrt{\frac{1+\epsilon}{1-\epsilon}}. \tag{3.47}$$

Putting them together, we have

$$\rho_{13}=-\frac{Q}{\omega}\frac{1}{1-\epsilon}\sqrt{\frac{\epsilon(1+\epsilon)}{2}}=-\frac{1}{1-\epsilon}\sqrt{\frac{Q^2}{\omega^2}\epsilon\frac{1+\epsilon}{2}}=-\frac{1}{1-\epsilon}\sqrt{\epsilon_L\frac{1+\epsilon}{2}}. \tag{3.48}$$

We can finally write the complete polarization density matrix by putting together Eq.ns (3.42), (3.39), (3.43) and (3.48):

$$\rho_{ij}=\frac{1}{1-\epsilon}\begin{pmatrix}\frac{1+\epsilon}{2} & 0 & -\sqrt{\epsilon_L\frac{1+\epsilon}{2}}\\ 0 & \frac{1-\epsilon}{2} & 0\\ -\sqrt{\epsilon_L\frac{1+\epsilon}{2}} & 0 & \epsilon_L\end{pmatrix}. \tag{3.49}$$

3.4 Model-independent parametrization of the hadronic tensor

In this section we are first going to see a model-independent procedure to parametrize the hadronic tensor using structure functions; then, we will expand Eq. (3.24) for the matrix element squared in the fully unpolarized case in terms of those structure functions. Finally, we will explain how these structure functions can be extracted from an arbitrary hadronic tensor.

3.4.1 Parametrization with structure functions

Since the hadronic tensor $W^{\mu\nu}$ just involves hadronic variables, the only four-momenta it can depend on are q, P, P' and p_1'; further, energy-momentum conservation fixes one of them: we will eliminate $P'=q+P-p_1'$ and keep q, P and p_1' as our three independent variables. We will also assume a parity conserving current, which forbids the linear dependence of $W^{\mu\nu}$ on the totally antisymmetric tensor. It follows from these

considerations that $W^{\mu\nu}$ must have the form

$$\begin{aligned} W^{\mu\nu} =& W_1 g^{\mu\nu} + W_2 q^\mu q^\nu + W_3 p_1'^\mu p_1'^\nu + W_4 P^\mu P^\nu + W_5 q^\mu p_1'^\nu + W_6 p_1'^\mu q^\nu + \\ &+ W_7 q^\mu P^\nu + W_8 P^\mu q^\nu + W_9 p_1'^\mu P^\nu + W_{10} P^\mu p_1'^\nu, \end{aligned} \tag{3.50}$$

where the W_j, $(j = 1, 2, ..., 10)$ are called structure functions. Another constraint comes from current conservation:

$$q_\mu W^{\mu\nu} = 0, \qquad q_\nu W^{\mu\nu} = 0. \tag{3.51}$$

Imposing this on (3.50) results in six equations, one of which is linearly dependent on the other five: this leaves us with only five independent structure functions.

However, it is easier to build $W^{\mu\nu}$ directly form current-conserving terms. Notice that, given a tensor with n indices $t^{\mu_1,\dots,\mu_n}$, it is possible to construct its current-conserving counterpart $T^{\mu_1,\dots,\mu_n}$, which automatically satisfies $q_\mu T^{\mu,\mu_2,\dots,\mu_n} = 0$, as follows:

$$T^{\mu_1,\dots,\mu_n} = t^{\mu_1,\dots,\mu_n} + t^{\mu,\mu_2,\dots,\mu_n} q_\mu \frac{q^{\mu_1}}{Q^2}, \tag{3.52}$$

Applying this procedure to q gives 0, while applying it to $g^{\mu\nu}$, P^μ and $p_1'^\mu$, respectively, results in the following tensors:

$$G^{\mu\nu} = g^{\mu\nu} + \frac{q^\mu q^\nu}{Q^2} \tag{3.53a}$$

$$A^\mu = P^\mu + \frac{P \cdot q}{Q^2} q^\mu \tag{3.53b}$$

$$B^\mu = p_1'^\mu + \frac{p_1' \cdot q}{Q^2} q^\mu. \tag{3.53c}$$

We can now write $W^{\mu\nu}$ as a combination of the tensors above, which leaves us with five structure functions, as expected:

$$W^{\mu\nu} = W_1 G^{\mu\nu} + W_2 A^\mu A^\nu + W_3 B^\mu B^\nu + W_4 (A^\mu B^\nu + B^\mu A^\nu) + W_5 (A^\mu B^\nu - B^\mu A^\nu). \tag{3.54}$$

Here, for the last two terms, we have separated the symmetric and antisymmetric part, and of course the structure functions have been redefined from the ones in Eq. (3.50).

3.4.2 Expansion of the matrix element

It is now straightforward to compute the matrix element squared by contracting the above hadronic tensor with the leptonic one (Eq. (3.24)). For the fully unpolarized case we have

$$|\mathcal{M}|^2 = \left(\frac{e^2}{Q^2}\right)^2 4Q^2 [\rho_{11} W^{11} + \rho_{22} W^{22} + \rho_{33} W^{33} + \rho_{13} (W^{13} + W^{31})]. \tag{3.55}$$

We will now express the above formula in terms of the structure functions. To do so, let us first compute the relevant components of $G^{\mu\nu}$, A^μ and B^μ: since, in the laboratory frame, the momenta are given by

$$q = (\omega, 0, 0, |\mathbf{q}|) \tag{3.56a}$$

$$P = (M_A, 0, 0, 0) \tag{3.56b}$$

$$p_1' = \left(E_{p_1'}, \sqrt{E_{p_1'}^2 - m_K^2}(\sin\theta_1' \cos\phi_1', \sin\theta_1' \sin\phi_1', \cos\theta_1')\right), \tag{3.56c}$$

we have

$$G^{11} = -1, \quad G^{22} = -1, \quad G^{33} = \frac{\omega^2}{Q^2}, \quad G^{13} = 0, \tag{3.57a}$$

$$A^1 = 0, \quad A^2 = 0, \quad A^3 = \frac{M_A \omega |\mathbf{q}|}{Q^2}, \tag{3.57b}$$

$$B^1 = \sqrt{E_{p_1'}^2 - m_K^2}\sin\theta_1' \cos\phi_1', \quad B^2 = \sqrt{E_{p_1'}^2 - m_K^2}\sin\theta_1' \sin\phi_1', \tag{3.57c}$$

$$B^3 = \frac{\omega}{Q^2}\left(|\mathbf{q}| E_{p_1'} - \omega\sqrt{E_{p_1'}^2 - m_K^2}\cos\theta_1'\right) \equiv \frac{\omega}{Q^2} b. \tag{3.57d}$$

Inserting these into Eq. (3.54) allows us to express the components of the hadronic tensor in terms of the structure functions; the components we need are

$$W^{11} = -W_1 + W_3(E_{p_1'}^2 - m_K^2)\sin^2\theta_1' \cos^2\phi_1', \tag{3.58a}$$

$$W^{22} = -W_1 + W_3(E_{p_1'}^2 - m_K^2)\sin^2\theta_1' \sin^2\phi_1', \tag{3.58b}$$

$$W^{33} = W_1\frac{\omega^2}{Q^2} + W_2\left(\frac{M_A\omega|\mathbf{q}|}{Q^2}\right)^2 + W_3\left(\frac{\omega b}{Q^2}\right)^2 + 2W_4\frac{M_A\omega^2|\mathbf{q}|}{Q^4}b, \tag{3.58c}$$

$$W^{13} + W^{31} = 2\frac{\omega}{Q^2}\sin\theta_1' \cos\phi_1'\sqrt{E_{p_1'}^2 - m_K^2}(W_3 b + W_4 M_A|\mathbf{q}|). \tag{3.58d}$$

We can finally insert these expressions into Eq. (3.55) to find the matrix element squared:

$$\begin{aligned}|\mathcal{M}|^2 = \frac{4e^4}{Q^2(1-\epsilon)}\Bigg[&\frac{1}{2}(-2W_1 + W_3(E_{p_1'}^2 - m_K^2)\sin^2\theta_1') \\ &+ \frac{\epsilon}{2}W_3(E_{p_1'}^2 - m_K^2)\sin^2\theta_1'(\cos^2\phi_1' - \sin^2\phi_1') \\ &+ \epsilon W_1 + \epsilon W_2\frac{M_A^2|\mathbf{q}|^2}{Q^2} + \epsilon W_3\frac{b^2}{Q^2} + 2\epsilon W_4\frac{M_A|\mathbf{q}|b}{Q^2} \\ &- \sqrt{2\epsilon(1+\epsilon)}\frac{\sqrt{E_{p_1'}^2 - m_K^2}}{Q}\sin\theta_1' \cos\phi_1'(W_3 b + W_4 M_A|\mathbf{q}|)\Bigg].\end{aligned} \tag{3.59}$$

This can be simplified to

$$|\mathcal{M}|^2 = \frac{4e^4}{Q^2(1-\epsilon)}\Bigg[W_1(\epsilon-1) + W_2\epsilon\frac{M_A^2|\mathbf{q}|^2}{Q^2} + W_3(E_{p_1'}^2 - m_K^2)\frac{\sin^2\theta_1'}{2}(1+\epsilon\cos 2\phi_1') \\ + W_4\epsilon\frac{M_A|\mathbf{q}|b}{Q^2} + (W_3 b + W_4 M_A|\mathbf{q}|)\left(\epsilon\frac{b}{Q^2} - \sqrt{2\epsilon(1+\epsilon)}\frac{\sqrt{E_{p_1'}^2 - m_K^2}}{Q}\sin\theta_1'\cos\phi_1'\right)\Bigg]. \tag{3.60}$$

3.4.3 Extracting structure functions from a hadronic tensor

Now, let us see how one can extract the structure functions from a given (model-dependent) hadronic tensor $W^{\mu\nu}$. From (3.54), we can write the symmetric part of the hadronic tensor as

$$W_s^{\mu\nu} = \sum_{i=1}^{4} W_i u_i^{\mu\nu}, \tag{3.61}$$

where $u_i^{\mu\nu} \equiv \{G^{\mu\nu}, A^\mu A^\nu, B^\mu B^\nu, (A^\mu B^\nu + B^\mu A^\nu)\}$. If we multiply the above equation by $u_{j\,\mu\nu}$ on both sides, we get

$$W_s^{\mu\nu} u_{j\,\mu\nu} = \sum_{i=1}^{4} W_i u_i^{\mu\nu} u_{j\,\mu\nu} \equiv \sum_{i=1}^{4} U_{ji} W_i, \tag{3.62}$$

where we have defined the symmetric matrix

$$U_{ij} = U_{ji} = u_i^{\mu\nu} u_{j\,\mu\nu}. \tag{3.63}$$

Let us rewrite Eq. (3.62) in a matrix-vector form:

$$\overrightarrow{W_u} = U\overrightarrow{W}, \tag{3.64}$$

where the components of the vectors are $(\overrightarrow{W_u})_i = W_s^{\mu\nu} u_{i\,\mu\nu}$, $(\overrightarrow{W})_i = W_i$ and U is the matrix whose elements are the ones in Eq. (3.63). Thus, in order to extract the structure functions, we need to invert the above equation:

$$\overrightarrow{W} = U^{-1}\overrightarrow{W_u}. \tag{3.65}$$

In order to get an explicit form of the U matrix, let us compute the contractions between the $G^{\mu\nu}$, A^μ and B^μ tensors:

$$G_{\mu\nu}G^{\mu\nu} = 3 \tag{3.66a}$$

$$G_{\mu\nu}A^\mu A^\nu = A_\mu A^\mu = A^2 = M_A^2\frac{|\mathbf{q}|^2}{Q^2} \tag{3.66b}$$

$$G_{\mu\nu}B^\mu B^\nu = B_\mu B^\mu = B^2 = m_K^2 + \left(\frac{|\mathbf{q}|b}{\omega Q} - \frac{E_{p_1'}Q}{\omega}\right)^2 \tag{3.66c}$$

$$G_{\mu\nu}A^\mu B^\nu = A_\mu B^\mu = A\cdot B = \frac{M_A|\mathbf{q}|b}{Q^2}. \tag{3.66d}$$

Note that, owing to the current conservation property of these tensors, $G_{\mu\nu}$ acts on A^μ and B^μ as the normal Minkowski metric. Then, using the definition (3.63), the U matrix takes the form

$$U = \begin{pmatrix} 3 & A^2 & B^2 & 2A\cdot B \\ A^2 & A^4 & (A\cdot B)^2 & 2A^2(A\cdot B) \\ B^2 & (A\cdot B)^2 & B^4 & 2B^2(A\cdot B) \\ 2A\cdot B & 2A^2(A\cdot B) & 2B^2(A\cdot B) & 2A^2B^2 + 2(A\cdot B)^2 \end{pmatrix}. \tag{3.67}$$

Its inverse U^{-1} is easily obtained with a symbolic calculation software, and its elements are listed below.

$$\begin{aligned}
(U^{-1})_{00} &= 1 \\
(U^{-1})_{01} = (U^{-1})_{10} &= \frac{-2A^4B^6 + 4A^2B^4(A\cdot B)^2 - 2B^2(A\cdot B)^4}{2A^6B^6 - 6A^4B^4(A\cdot B)^2 + 6A^2B^2(A\cdot B)^4 - 2(A\cdot B)^6} \\
(U^{-1})_{02} = (U^{-1})_{20} &= \frac{-2A^6B^4 + 4A^4B^2(A\cdot B)^2 - 2A^2(A\cdot B)^4}{2A^6B^6 - 6A^4B^4(A\cdot B)^2 + 6A^2B^2(A\cdot B)^4 - 2(A\cdot B)^6} \\
(U^{-1})_{03} = (U^{-1})_{30} &= \frac{2A^4B^4(A\cdot B) - 4A^2B^2(A\cdot B)^3 + 2(A\cdot B)^5}{2A^6B^6 - 6A^4B^4(A\cdot B)^2 + 6A^2B^2(A\cdot B)^4 - 2(A\cdot B)^6} \\
(U^{-1})_{11} &= \frac{4A^2B^6 - 4B^4(A\cdot B)^2}{2A^6B^6 - 6A^4B^4(A\cdot B)^2 + 6A^2B^2(A\cdot B)^4 - 2(A\cdot B)^6} \\
(U^{-1})_{12} = (U^{-1})_{21} &= \frac{2A^4B^4 - 2(A\cdot B)^4}{2A^6B^6 - 6A^4B^4(A\cdot B)^2 + 6A^2B^2(A\cdot B)^4 - 2(A\cdot B)^6} \\
(U^{-1})_{13} = (U^{-1})_{31} &= \frac{4B^2(A\cdot B)^3 - 4A^2B^4(A\cdot B)}{2A^6B^6 - 6A^4B^4(A\cdot B)^2 + 6A^2B^2(A\cdot B)^4 - 2(A\cdot B)^6} \\
(U^{-1})_{22} &= \frac{4A^6B^2 - 4A^4(A\cdot B)^2}{2A^6B^6 - 6A^4B^4(A\cdot B)^2 + 6A^2B^2(A\cdot B)^4 - 2(A\cdot B)^6} \\
(U^{-1})_{23} = (U^{-1})_{32} &= \frac{4A^2(A\cdot B)^3 - 4A^4B^2(A\cdot B)}{2A^6B^6 - 6A^4B^4(A\cdot B)^2 + 6A^2B^2(A\cdot B)^4 - 2(A\cdot B)^6} \\
(U^{-1})_{33} &= \frac{A^4B^4 + 2A^2B^2(A\cdot B)^2 - 3(A\cdot B)^4}{2A^6B^6 - 6A^4B^4(A\cdot B)^2 + 6A^2B^2(A\cdot B)^4 - 2(A\cdot B)^6}
\end{aligned} \tag{3.68}$$

3.5 Model for the hadronic tensor

3.5.1 Integration of the elementary current

In order to model the hadronic tensor $W^{\mu\nu}$, we are going to employ some approximations. First, since we consider a high photon momentum, we will assume that it interacts with just one bound nucleon (see Fig. 3.2). This allows us to neglect two- and many-body components of the current operator. We will also neglect rescattering processes of the produced kaon and Λ, as well as kaon distortion effects.
We are going to denote the four-momenta of the bound proton and Λ $p^\mu = (E_p, \mathbf{p})$ and $p_2'^\mu = (E_{p_2'}, \mathbf{p}_2')$, respectively. Recalling that we had set $w^\mu_{\alpha_A,\alpha_Y} = \langle K^+{}_\Lambda A| J^\mu(q) |A\rangle_{\alpha_A,\alpha_Y}$, the above approximations allow us to rewrite it as

$$\begin{aligned} w^\mu_{\alpha_A,\alpha_Y} &= \int d^3\mathbf{p}_2'\, d^3\mathbf{p}\, \delta^3\left(\mathbf{q}+\mathbf{p}-\mathbf{p}_1'-\mathbf{p}_2'\right) \overline{\mathcal{U}}_{\alpha_\Lambda}\left(\mathbf{p}_2'\right) \widehat{J}^\mu(q)\, \mathcal{U}_{\alpha_p}(\mathbf{p}) \\ &= \int d^3\mathbf{p}\, \overline{\mathcal{U}}_{\alpha_\Lambda}\left(\mathbf{q}+\mathbf{p}-\mathbf{p}_1'\right) \widehat{J}^\mu(q)\, \mathcal{U}_{\alpha_p}(\mathbf{p}) \\ &= \int_0^{p_{\max}} dp \int_0^{\pi} d\theta \int_0^{2\pi} d\phi \left(p^2 \sin\theta\right) \overline{\mathcal{U}}_{\alpha_\Lambda}\left(\mathbf{q}+\mathbf{p}-\mathbf{p}_1'\right) \widehat{J}^\mu(q)\, \mathcal{U}_{\alpha_p}(\mathbf{p}) \end{aligned} \tag{3.69}$$

where $\mathcal{U}_{\alpha_p}$ and $\mathcal{U}_{\alpha_\Lambda}$ are the spinor wavefunctions of the bound proton and Λ, respectively, and $\widehat{J}^\mu(q)$ is the current operator for the elementary process $\gamma^* + p \to K^+ + \Lambda$, with γ^* the virtual photon; $p_{\max}$ is the maximum momentum for which the momentum space wavefunctions are still appreciable.

Finally, all that is left to do in order to obtain the hadronic tensor for this model is to insert $w^\mu_{\alpha_A,\alpha_Y}$, calculated with the formula above, into Eq. (3.17).

3.5.2 Momentum space wavefunctions for bound spinors

Let us write down the explicit form of the bound spinor wavefunctions $\mathcal{U}(\mathbf{p})$. To do this, we start from the coordinate representation

$$\mathcal{U}_{E\kappa m}(\mathbf{x}) = \begin{pmatrix} \dfrac{g_{E\kappa}(r)}{r}\mathcal{Y}_{\kappa m}(\hat{\mathbf{x}}) \\ \dfrac{i f_{E\kappa}(r)}{r}\mathcal{Y}_{-\kappa m}(\hat{\mathbf{x}}) \end{pmatrix}, \tag{3.70}$$

where $\hat{\mathbf{x}}$ is the unit vector associated to the position $\mathbf{x}$, E is the binding energy of the spinor, m is the total magnetic quantum number (i.e. associated with the total angular momentum j), and κ is the generalized angular momentum.

The relations between κ, j and l are:

$$j = |\kappa| - \frac{1}{2}, \qquad l = \begin{cases} \kappa & \text{if } \kappa > 0 \\ -1-\kappa & \text{if } \kappa < 0 \end{cases}, \tag{3.71}$$

or equivalently

$$\kappa = \begin{cases} j + \frac{1}{2} = l & \text{if } j = l - \frac{1}{2} \\ -j - \frac{1}{2} = -l - 1 & \text{if } j = l + \frac{1}{2} \end{cases}. \tag{3.72}$$

Note that $j(-\kappa) = j(\kappa)$, while $l(-\kappa) = l(\kappa) \pm 1$, the upper and lower signs corresponding to the cases $j(\kappa) = l(\kappa) \pm \frac{1}{2}$. In other words, switching from κ to $-\kappa$ leaves j unchanged, while l changes to the other orbital angular momentum that can give rise to the same total j, according to the summation rules of angular momentum. One can easily check that, for both cases $j(\kappa) = l(\kappa) \pm \frac{1}{2}$, the following equality holds:

$$l(-\kappa) = 2j(\kappa) - l(\kappa). \tag{3.73}$$

The $\mathcal{Y}_{\kappa m}(\hat{\mathbf{x}})$ in Eq. (3.70) are the spinor spherical harmonics, which have the form

$$\begin{aligned} \mathcal{Y}_{\kappa m}(\hat{\mathbf{x}}) &= \sum_{s'_z = \pm 1/2} (l, m - s'_z, \tfrac{1}{2}, s'_z | jm) Y_{l, m-s'_z}(\hat{\mathbf{x}}) \chi_{s'_z} \\ &= \begin{pmatrix} (l, m - \frac{1}{2}, \frac{1}{2}, \frac{1}{2} | j, m) Y_{l,m-1/2}(\hat{\mathbf{x}}) \\ (l, m + \frac{1}{2}, \frac{1}{2}, -\frac{1}{2} | j, m) Y_{l,m+1/2}(\hat{\mathbf{x}}) \end{pmatrix}; \end{aligned} \tag{3.74}$$

The expressions for the Clebsch-Gordan coefficients appearing in the equation above are, for the cases $j = l \pm \frac{1}{2}$,

$$\begin{aligned} (l, m - \tfrac{1}{2}, \tfrac{1}{2}, \tfrac{1}{2} | l \pm \tfrac{1}{2}, m) &= \pm \sqrt{\frac{l \pm m + \frac{1}{2}}{2l+1}} \\ (l, m + \tfrac{1}{2}, \tfrac{1}{2}, -\tfrac{1}{2} | l \pm \tfrac{1}{2}, m) &= \sqrt{\frac{l \mp m + \frac{1}{2}}{2l+1}}. \end{aligned} \tag{3.75}$$

Let us also mention that the wavefunctions in Eq. (3.70) are normalized as

$$\int d^3\mathbf{x}\, \mathcal{U}^\dagger_{E\kappa m}(\mathbf{x}) \mathcal{U}_{E\kappa m}(\mathbf{x}) = \int d^3 r \left(g^2(r) + f^2(r) \right) = 1. \tag{3.76}$$

To get the momentum space version of Eq. (3.70), one has to take the Fourier transform

$$\mathcal{U}_{E\kappa m}(\mathbf{p}) = \frac{1}{(2\pi)^{3/2}} \int d^3\mathbf{x}\, e^{-i\mathbf{p}\cdot\mathbf{x}} \mathcal{U}_{E\kappa m}(\mathbf{x}), \tag{3.77}$$

which can be simplified using three mathematical identities. The first one is the partial waves decomposition of a plane wave

$$e^{-i\mathbf{p}\cdot\mathbf{x}} = 4\pi \sum_{l=0}^{\infty} (-i)^l j_l(pr) \sum_{m=-l}^{l} Y^*_{lm}(\hat{\mathbf{x}}) Y_{lm}(\hat{\mathbf{p}}), \tag{3.78}$$

where $j_l(x)$ denotes the spherical Bessel function of order l; the second one is the normalization of spherical harmonics

$$\int d\Omega\, Y^*_{lm}(\Omega) Y_{l'm'}(\Omega) = \delta_{ll'}\delta_{mm'}; \tag{3.79}$$

the third one is a recurrence relation for spinor spherical harmonics [36]:

$$\boldsymbol{\sigma}\cdot\hat{\mathbf{x}}\,\mathcal{Y}_{\kappa m}(\hat{\mathbf{x}}) = -\mathcal{Y}_{-\kappa m}(\hat{\mathbf{x}}), \tag{3.80}$$

where $\boldsymbol{\sigma}$ is the vector containing the three Pauli matrices.
We will start by taking the Fourier transform of the upper part of $\mathcal{U}_{E\kappa m}(\mathbf{x})$: inserting Eq. (3.78) into (3.77) we obtain

$$\begin{aligned}
&\frac{1}{(2\pi)^{3/2}}\int d^3\mathbf{x}\, e^{-i\mathbf{p}\cdot\mathbf{x}}\frac{g_{E\kappa}(r)}{r}\mathcal{Y}_{\kappa m}(\hat{\mathbf{x}}) = \\
=&\frac{4\pi}{(2\pi)^{3/2}}\sum_{l'=0}^{\infty}(-i)^{l'}\int_0^\infty dr\, r^2 j_{l'}(pr)\sum_{m'=-l'}^{l'}\int d\Omega_x\, Y^*_{l'm'}(\hat{\mathbf{x}})Y_{l'm'}(\hat{\mathbf{p}})\frac{g_{E\kappa}(r)}{r}\mathcal{Y}_{\kappa m}(\hat{\mathbf{x}}) = \\
=&\sqrt{\frac{2}{\pi}}(-i)^l\,\mathcal{Y}_{\kappa m}(\hat{\mathbf{p}})\int_0^\infty dr\, r g(r) j_l(pr),
\end{aligned} \tag{3.81}$$

where the second line follows from using Eq. (3.80) and the fact that $\mathcal{Y}_{\kappa m}$ contains the spherical harmonic of degree l. Similarly, for the lower part of $\mathcal{U}_{E\kappa m}(\mathbf{x})$ we have

$$\begin{aligned}
&\frac{i}{(2\pi)^{3/2}}\int d^3\mathbf{x}\, e^{-i\mathbf{p}\cdot\mathbf{x}}\frac{f_{E\kappa}(r)}{r}\mathcal{Y}_{-\kappa m}(\hat{\mathbf{x}}) = \\
=&\frac{4\pi i}{(2\pi)^{3/2}}\sum_{l'=0}^{\infty}(-i)^{l'}\int_0^\infty dr\, r^2 j_{l'}(pr)\sum_{m'=-l'}^{l'}\int d\Omega_x\, Y^*_{l'm'}(\hat{\mathbf{x}})Y_{l'm'}(\hat{\mathbf{p}})\frac{f_{E\kappa}(r)}{r}\mathcal{Y}_{-\kappa m}(\hat{\mathbf{x}}) = \\
=&\mathrm{sgn}(-\kappa)\sqrt{\frac{2}{\pi}}(-i)^l\,\mathcal{Y}_{-\kappa m}(\hat{\mathbf{p}})\int_0^\infty dr\, r f(r) j_{2j-l}(pr) \\
=&\mathrm{sgn}(\kappa)\sqrt{\frac{2}{\pi}}(-i)^l\,\boldsymbol{\sigma}\cdot\hat{\mathbf{p}}\,\mathcal{Y}_{\kappa m}(\hat{\mathbf{p}})\int_0^\infty dr\, r f(r) j_{2j-l}(pr),
\end{aligned} \tag{3.82}$$

where, once again, the second line follows from using Eq. (3.80) and the fact that $\mathcal{Y}_{-\kappa m}$ contains the spherical harmonic of degree $2j-l$; additionally, one can easily check that $(-i)^{2j-l-1} = (-i)^l\,\mathrm{sgn}(-\kappa)$ for both cases $\kappa > 0$ and $\kappa < 0$.

Putting back together the upper and lower parts of the bound spinor wavefunction in momentum space, we finally obtain

$$\begin{aligned}
\mathcal{U}_{E\kappa m}(\mathbf{p}) &= \sqrt{\frac{2}{\pi}}(-i)^l\begin{pmatrix} \left[\int_0^\infty dr\, r g(r) j_l(pr)\right]\,\mathcal{Y}_{\kappa m}(\hat{\mathbf{p}}) \\ \mathrm{sgn}(\kappa)\left[\int_0^\infty dr\, r f(r) j_{2j-l}(pr)\right]\,\boldsymbol{\sigma}\cdot\hat{\mathbf{p}}\,\mathcal{Y}_{\kappa m}(\hat{\mathbf{p}}) \end{pmatrix} \\
&\equiv \sqrt{\frac{2}{\pi}}(-i)^l\begin{pmatrix} g(p)\,\mathcal{Y}_{\kappa m}(\hat{\mathbf{p}}) \\ \mathrm{sgn}(\kappa) f(p)\,\boldsymbol{\sigma}\cdot\hat{\mathbf{p}}\,\mathcal{Y}_{\kappa m}(\hat{\mathbf{p}}) \end{pmatrix}.
\end{aligned} \tag{3.83}$$

These wavefunctions are normalized as

$$\int d^3\mathbf{p}\, \mathcal{U}^{\dagger}_{E\kappa m}(\mathbf{p})\, \mathcal{U}_{E\kappa m}(\mathbf{p}) = 1 \;\Rightarrow\; \int d^3p\, p^2 \left(g^2(p) + f^2(p)\right) = \frac{\pi}{2}. \tag{3.84}$$

Note that, if we fix the orbital to which the proton or Λ belongs, the above wavefunction still depends on the magnetic quantum number m: this means that, when building the hadronic tensor using Eq. (3.17), we will have to sum over the magnetic quantum numbers of the proton and Λ.

Chapter 4

The elementary process

We have seen that, in order to evaluate the hadronic current and tensor, one of the key ingredients is the current operator $\widehat{J}^\mu$ for the elementary process $\gamma^*(q) + p(p) \to K(p'_1) + \Lambda(p'_2)$. In this section we will see how to model this operator, but first we need to know how the kinematics of the elementary process is fixed.

4.1 Kinematics of the elementary process

A full knowledge of the kinematical variables of the $\gamma^* + p \to K + \Lambda$ process is needed in order to evaluate the associated current operator. Given the initial four-momenta q and p, then, due to energy-momentum conservation, the kinematics of the reaction is fixed if we provide two variables for the final state. In this work, we will choose these variables to be the kaon's polar and azimuthal angles (i.e. θ'_1 and ϕ'_1).

We will now derive the expression for the kaon energy $E_{p'_1}$. Recall that the virtual photon momentum is fixed by the leptonic part of the process as

$$q^\mu = (\omega, 0, 0, |\mathbf{q}|). \tag{4.1}$$

For the proton, since its wavefunction is given in terms of its three-momentum in polar coordinates, we will parametrize the four-momentum in terms of the same variables:

$$p^\mu = \left(\sqrt{|\mathbf{p}|^2 + m_p^2},\ |\mathbf{p}|\sin\theta\cos\phi,\ |\mathbf{p}|\sin\theta\sin\phi,\ |\mathbf{p}|\cos\theta\right). \tag{4.2}$$

Now, given θ'_1 and ϕ'_1, the energy of the outgoing kaon is determined by requiring that the following equations are simultaneously satisfied:

$$p'_2 = p + q - p'_1 \tag{4.3a}$$

$$(p'_2)^2 = m_\Lambda^2. \tag{4.3b}$$

The first equation corresponds to momentum conservation, while the second one is the mass-shell condition for the bound Λ. Let us also fix the form of the kaon four-momentum as

$$p_1'^{\mu} = \left(E_{p_1'},\, \sqrt{E_{p_1'}^2 - m_K^2}\sin\theta_1'\cos\phi_1',\, \sqrt{E_{p_1'}^2 - m_K^2}\sin\theta_1'\sin\phi_1',\, \sqrt{E_{p_1'}^2 - m_K^2}\cos\theta_1'\right). \tag{4.4}$$

We can plug this equation into (4.3a) in order to find a more explicit expression for the Λ four-momentum

$$\begin{aligned} p_2'^{\mu} = \Big(&\sqrt{|\mathbf{p}|^2 + m_p^2} + \omega - E_{p_1'}, \\ &|\mathbf{p}|\sin\theta\cos\phi - \sqrt{E_{p_1'}^2 - m_K^2}\sin\theta_1'\cos\phi_1', \\ &|\mathbf{p}|\sin\theta\sin\phi - \sqrt{E_{p_1'}^2 - m_K^2}\sin\theta_1'\sin\phi_1', \\ &|\mathbf{p}|\cos\theta + |\mathbf{q}| - \sqrt{E_{p_1'}^2 - m_K^2}\cos\theta_1'\Big) \end{aligned} \tag{4.5}$$

and then impose (4.3b): this gives

$$\begin{aligned} 0 =& m_K^2 - m_\Lambda^2 + (q+p)^2 - 2E_{p_1'}\Big(\omega + \sqrt{|\mathbf{p}|^2 + m_p^2}\Big) + \\ &+ 2\sqrt{E_{p_1'}^2 - m_K^2}\Big[|\mathbf{q}|\cos\theta_1' + |\mathbf{p}|(\sin\theta\sin\theta_1'\cos(\phi - \phi_1') + \cos\theta\cos\theta_1')\Big] \end{aligned} \tag{4.6}$$

For the sake of brevity, let us denote

$$\alpha \equiv m_K^2 - m_\Lambda^2 + (q+p)^2 \tag{4.7a}$$

$$\beta \equiv |\mathbf{q}|\cos\theta_1' + |\mathbf{p}|[\sin\theta\sin\theta_1'\cos(\phi - \phi_1') + \cos\theta\cos\theta_1'] \tag{4.7b}$$

so that Eq. (4.6) becomes

$$2\beta\sqrt{E_{p_1'}^2 - m_K^2} = 2\Big(\omega + \sqrt{|\mathbf{p}|^2 + m_p^2}\Big)E_{p_1'} - \alpha. \tag{4.8}$$

Squaring both sides of this equation gives a second-degree equation in $E_{p_1'}$ with an additional condition:

$$\begin{cases} \left[\Big(\omega + \sqrt{|\mathbf{p}|^2 + m_p^2}\Big)^2 - \beta^2\right]E_{p_1'}^2 - \alpha\Big(\omega + \sqrt{|\mathbf{p}|^2 + m_p^2}\Big)E_{p_1'} + \dfrac{\alpha^2}{4} + \beta^2 m_K^2 = 0 \\ \dfrac{2\left(\omega + \sqrt{|\mathbf{p}|^2 + m_p^2}\right)E_{p_1'} - \alpha}{\beta} \geq 0. \end{cases} \tag{4.9}$$

The solution is (naming $\sqrt{|\mathbf{p}|^2 + m_p^2} = E_p$)

$$\begin{cases} E_{p_1'} = \dfrac{\alpha(\omega + E_p) \pm \sqrt{\alpha^2(\omega + E_p)^2 + (\alpha^2 + 4\beta^2 m_K^2)[\beta^2 - (\omega + E_p)^2]}}{2[(\omega + E_p)^2 - \beta^2]} \\ \qquad = \dfrac{\alpha(\omega + E_p) \pm \sqrt{\alpha^2\beta^2 - 4\beta^2 m_K^2[(\omega + E_p)^2 - \beta^2]}}{2[(\omega + E_p)^2 - \beta^2]} \\ \dfrac{2\,(\omega + E_p)\,E_{p_1'} - \alpha}{\beta} \geq 0. \end{cases} \tag{4.10}$$

Now both the kaon and Λ four-momenta are fixed: for the kaon, one simply needs to insert the energy of Eq. (4.10) into Eq. (4.4), while the Λ four-momentum is obtained via Eq. (4.3a).

4.2 Elementary observables

Since all the models we are about to see are fitted to experimental data, we need to briefly mention which are the observables for the elementary process and how they are calculated. Note that, unlike what we have seen for the nuclear reaction, the elementary observables are usually evaluated in the center of mass frame.

The first observable is, of course, the differential cross section. Following a procedure analogous to the one we have described in Section 3.1, factorizing the matrix element as we have done in Section 3.2 and parametrizing the leptonic tensor as in Section 3.3, the triple differential cross section for the elementary electroproduction process with unpolarized electron beams can be written as [6]

$$\begin{aligned} \frac{d^3\sigma}{dE_{k'}d\Omega' d\Omega_1'} =& \frac{1}{(2\pi)^3}\frac{\alpha^2}{Q^2(1-\epsilon)}\frac{E_{k'}m_p}{k\cdot p}\frac{m_\Lambda |\mathbf{p}_1'|^2}{4E_{p_1'}E_{p_2'}R}\Big[(\tilde{W}^{11} + \tilde{W}^{22}) \\ &+ \epsilon(\tilde{W}^{11} - \tilde{W}^{22}) + 2\epsilon_L \tilde{W}^{33} - \sqrt{2\epsilon_L(1+\epsilon)}\left(\tilde{W}^{13} + \tilde{W}^{31}\right)\Big], \end{aligned} \tag{4.11}$$

where $\alpha = \frac{e^2}{4\pi}$, $R = \frac{|\mathbf{p}_1'|}{E_{p_1'}} - \frac{\mathbf{p}_1'\mathbf{p}_2'}{|\mathbf{p}_1'|E_{p_2'}}$, and

$$\tilde{W}^{\mu\nu} = \sum_{\text{spins}} \tilde{J}^\mu \tilde{J}^{\nu\,*} \tag{4.12}$$

is the hadronic tensor for the elementary process. Note that $\tilde{J}^\mu$ is not the elementary current operator that we need, e.g., to model the nuclear reaction; it is, instead, the

sandwich of the elementary current operator between free Dirac spinors for the incoming proton and outgoing Λ:

$$\tilde{J}^{\mu} = \overline{u}_{\Lambda} \widehat{J}^{\mu} u_p \tag{4.13}$$

Formula (4.11) is valid for any reference frame; let us now concentrate on the center of mass frame. It is common practice to define the effective photon energy E_γ and the virtual photon flux Γ as, respectively,

$$E_\gamma \equiv \omega + \frac{Q^2}{2m_p} \quad \text{and} \quad \Gamma \equiv \frac{\alpha}{2\pi^2 Q^2} \frac{E_\gamma}{1-\epsilon} \frac{E_{k'}}{E_k}. \tag{4.14}$$

It is now possible to separate the dependence on the angle ϕ_1' in Eq. (4.11) and rewrite it as

$$\frac{d^3\sigma}{dE_{k'} d\Omega' d\Omega_1'} = \Gamma \left[\frac{d\sigma_T}{d\Omega_1'} + \epsilon \frac{d\sigma_L}{d\Omega_1'} + \epsilon \frac{d\sigma_P}{d\Omega_1'} \cos 2\phi_1' + \sqrt{2\epsilon(1+\epsilon)} \frac{d\sigma_I}{d\Omega_1'} \cos \phi_1' \right], \tag{4.15}$$

where σ_T, σ_L, σ_P and σ_I are called transverse, longitudinal, polarization and interference cross sections, respectively, and are given by

$$\begin{aligned}
\frac{d\sigma_T}{d\Omega_1'} &= \frac{\alpha}{4\pi} \frac{m_\Lambda}{E_{p_2'}} \frac{|\mathbf{p}_1'|^2}{4 E_{p_1'} R} \frac{1}{E_\gamma} \left(\tilde{W}^{11} + \tilde{W}^{22} \right)_{\phi_1'=0}, \\
\frac{d\sigma_L}{d\Omega_1'} &= \frac{\alpha}{4\pi} \frac{m_\Lambda}{E_{p_2'}} \frac{|\mathbf{p}_1'|^2}{4 E_{p_1'} R} \frac{1}{E_\gamma} 2\frac{Q^2}{\omega^2} \left(\tilde{W}^{33} \right)_{\phi_1'=0}, \\
\frac{d\sigma_P}{d\Omega_1'} &= \frac{\alpha}{4\pi} \frac{m_\Lambda}{E_{p_2'}} \frac{|\mathbf{p}_1'|^2}{4 E_{p_1'} R} \frac{1}{E_\gamma} \left(\tilde{W}^{11} - \tilde{W}^{22} \right)_{\phi_1'=0}, \\
\frac{d\sigma_I}{d\Omega_1'} &= -\frac{\alpha}{4\pi} \frac{m_\Lambda}{E_{p_2'}} \frac{|\mathbf{p}_1'|^2}{4 E_{p_1'} R} \frac{1}{E_\gamma} \sqrt{\frac{Q^2}{\omega^2}} \left(\tilde{W}^{13} + \tilde{W}^{31} \right)_{\phi_1'=0}.
\end{aligned} \tag{4.16}$$

Experimental data may also be presented in terms of

$$\frac{d\sigma_U}{d\Omega_1'} \equiv \frac{d\sigma_T}{d\Omega_1'} + \epsilon \frac{d\sigma_L}{d\Omega_1'}. \tag{4.17}$$

Another common practice is to express the elementary current and the above cross section components in terms of the so-called CGLN (Chew-Goldberg-Low-Nambu) amplitudes f_i, $i = 1, 2, ..., 6$ [12]. If $\boldsymbol{\varepsilon}$ is the polarization vector of the photon, then one can write

$$\begin{aligned}
\boldsymbol{\varepsilon} \cdot \widehat{\mathbf{J}} =& f_1 (\boldsymbol{\sigma} \cdot \boldsymbol{\varepsilon}) + i f_2 \left(\boldsymbol{\sigma} \cdot \hat{\mathbf{p}}_1' \right) \left[\boldsymbol{\sigma} \cdot (\hat{\mathbf{q}} \times \boldsymbol{\varepsilon}) \right] + f_3 (\boldsymbol{\sigma} \cdot \hat{\mathbf{q}}) \left(\hat{\mathbf{p}}_1' \cdot \boldsymbol{\varepsilon} \right) \\
&+ f_4 \left(\boldsymbol{\sigma} \cdot \hat{\mathbf{p}}_1' \right) \left(\hat{\mathbf{p}}_1' \cdot \boldsymbol{\varepsilon} \right) + f_5 (\boldsymbol{\sigma} \cdot \hat{\mathbf{q}}) (\hat{\mathbf{q}} \cdot \boldsymbol{\varepsilon}) + f_6 \left(\boldsymbol{\sigma} \cdot \hat{\mathbf{p}}_1' \right) (\hat{\mathbf{q}} \cdot \boldsymbol{\varepsilon}),
\end{aligned} \tag{4.18}$$

where $\hat{\mathbf{q}}$ and $\hat{\mathbf{p}}_1'$ are the unit vectors of the photon and kaon momentum, respectively.

Now the cross section components take the form

$$\begin{aligned}
\frac{d\sigma_{\mathrm{T}}}{d\Omega_1'} &= C\,\mathrm{Re}\left\{|f_1|^2+|f_2|^2-2f_1f_2^*\cos\theta_1'+\sin\theta_1'\left[\frac{1}{2}\left(|f_1|^2+|f_2|^2\right)\right.\right.\\
&\qquad\left.\left.+f_1f_4^*+f_2f_3^*+f_3f_4^*\cos\theta_1'\right]\right\}\\
\frac{d\sigma_{\mathrm{L}}}{d\Omega_1'} &= C\frac{Q^2}{\omega^2}\,\mathrm{Re}\left\{|\tilde{f}_5|^2+|\tilde{f}_6|^2+2\tilde{f}_5\tilde{f}_6^*\cos\theta_1'\right\}\\
\frac{d\sigma_{\mathrm{P}}}{d\Omega_1'} &= C\,\mathrm{Re}\left\{\frac{1}{2}\left(|f_3|^2+|f_4|^2\right)+f_1f_4^*+f_2f_3^*+f_4f_3^*\cos\theta_1'\right\}\\
\frac{d\sigma_{\mathrm{I}}}{d\Omega_1'} &= -C\sqrt{\frac{Q^2}{\omega^2}}\,\mathrm{Re}\left\{\left(f_1+f_4\right)\tilde{f}_6^*+\left(f_2+f_3\right)\tilde{f}_5^*+\left(f_3\tilde{f}_6^*+f_4\tilde{f}_5^*\right)\cos\theta_1'\right\},
\end{aligned}\tag{4.19}$$

where we have defined

$$\tilde{f}_5 = f_1+f_3\cos\theta_1'+f_5 \tag{4.20a}$$

$$\tilde{f}_6 = f_4\cos\theta_1'+f_6 \tag{4.20b}$$

and

$$C=\frac{\alpha}{4\pi}\frac{m_\Lambda\,|\mathbf{p}_1'|}{|\mathbf{q}|\sqrt{s}}. \tag{4.21}$$

When the (virtual) photon is polarized, other observables emerge. First, the cross section acquires two additional components:

$$\frac{d^3\sigma_{\mathrm{polarized}}}{dE_{k'}d\Omega'd\Omega_1'}=\frac{d^3\sigma_{\mathrm{unpolarized}}}{dE_{k'}d\Omega'd\Omega_1'}+\Gamma\left[h\sqrt{1-\epsilon^2}\frac{d\sigma_{P'}}{d\Omega_1'}\cos 2\phi_1'+h\sqrt{2\epsilon(1+\epsilon)}\frac{d\sigma_{I'}}{d\Omega_1'}\sin\phi_1'\right]. \tag{4.22}$$

Then, one can measure the Λ polarization P, the beam asymmetry Σ and the target polarization T. These are all expressed in terms of CGLN amplitudes; for example, for the first one we have

$$P=-\mathrm{Im}\left\{2f_1^*f_2+f_1^*f_3-f_2^*f_4-\left(f_2^*f_3-f_1^*f_4\right)\cos\theta_1'-f_3^*f_4\sin^2\theta_1'\right\}\sin\theta_1'. \tag{4.23}$$

4.3 Models for the elementary process: overview

Having established the formalism to treat the elementary process, we are ready to see which are the models that can describe the current operator. As we have seen in Section 2.3, there are two main types of approaches: QCD and hadrodynamical ones. Since it is extremely challenging to use the first at the energies of our interest, where QCD is non-perturbative, we are going to focus on the second approach.

One can distinguish two other categories of models: single-channel or coupled-channel approaches. In coupled-channel approaches one fully takes into account the interaction between the meson and the baryon in the final state, such as rescattering effects and interactions; this type of approach has the benefit to explicitly preserve unitarity, but of course the full treatment of the final state interaction is rather complicated. The simplified single-channel approaches, instead, neglect all higher-order effects; unitarity is restored, for example, with the help of energy-dependent decay widths. Additionally, the effective coupling constants of these models include part of the rescattering effects. Due to their simplicity, we are going to focus on single-channel approaches.

There are three main approaches to model the elementary process that are both hadrodynamical and single-channel: isobar models, Regge-plus-resonance (RPR) models and multipole approaches. In the following sections we are going to see their characteristics in more detail, particularly for the isobar models. Among isobar models, we will focus on the Kaon-MAID, since it is the one we will employ in our numerical calculations.

4.4 Isobar models

Isobar models use an effective meson-baryon Lagrangian to build the reaction amplitude as a sum of tree-level Feynman diagrams; neglecting higher order diagrams corresponds to neglecting, e.g., rescattering effects. Thus, the elementary process is viewed as an exchange of particles in the ground state (Born diagrams) or their resonances. Figure 4.1 depicts the Born diagrams for all possible reaction channels: we have an exchange of a proton in the s-channel, a kaon in the t-channel and a Λ or a Σ in the u-channel; for non-Born diagrams, one just needs to consider the exchange of resonances of these particles. The contact diagram is included whenever one needs to restore gauge invariance; this can happen, for example, when a pseudo-vector coupling is used or after the inclusion of hadron form factors. Nucleon resonances are the ones which are responsible for creating resonant structures in the observables, since the poles on the other diagrams are far from the physical region and cannot create peak-like structures.

4.4.1 The current operator

In isobar models, the current operator is built from these Feynman diagrams by using standard Feynman rules (see, e.g., [13]). Since Feynman rules contain Dirac γ matrices,

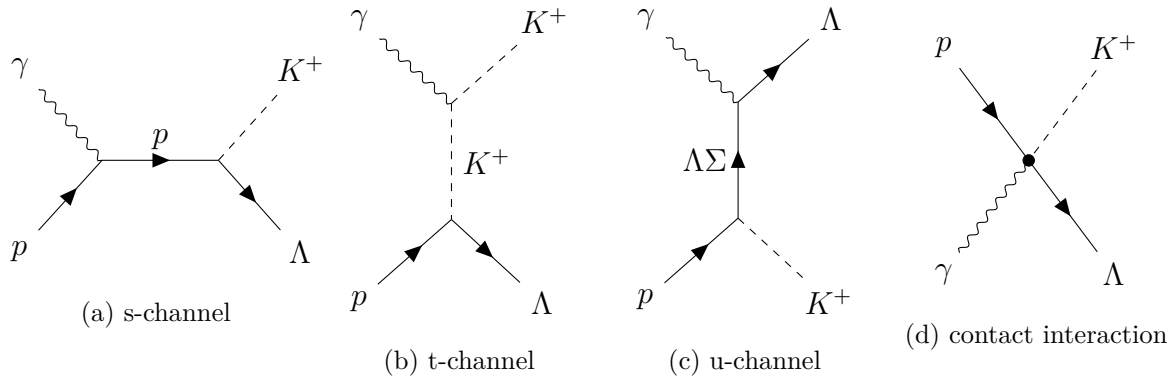

Figure 4.1: Feynman diagrams for the elementary process in the Born approximation. For non-Born diagrams, the exchanged particles are replaced by their resonances.

the current operator will be a 4×4 matrix. The current must also be gauge invariant (i.e. it must satisfy $\widehat{J}^\mu q_\mu = 0$), so it is useful to express it as a linear combination of a basis of six gauge invariant matrices M_i:

$$\widehat{J}^\mu = \sum_{i=1}^{6} A_i M_i^\mu. \tag{4.24}$$

The coefficients A_i are also Lorentz invariant, and are called Lorentz invariant amplitudes. Of course, there are many possibilities for the choice of the basis $\{M_i\}$; a popular one is

$$\begin{aligned}
M_1^\mu &= \tfrac{1}{2}\gamma^5(\gamma^\mu \not{q} - \not{q}\gamma^\mu) \\
M_2^\mu &= \tfrac{1}{2}\gamma^5[(p+p_2')\cdot q\,(2p_1'-q)^\mu - (2p_1'-q)\cdot q\,(p+p_2')^\mu] \\
M_3^\mu &= \gamma^5(p_1'\cdot q\,\gamma^\mu - \not{q}p_1'^\mu) \\
M_4^\mu &= i\epsilon_{\alpha\beta\lambda\nu}\gamma^\alpha p_1'^\beta q^\nu g^{\lambda\mu} \\
M_5^\mu &= \gamma^5\left(q^2 p_1'^\mu - p_1'\cdot q\, q^\mu\right) \\
M_6^\mu &= \gamma^5\left(q^\mu \not{q} - q^2\gamma^\mu\right)
\end{aligned} \tag{4.25}$$

Extracting the A_i for a specified model is also useful because the CGLN amplitudes can be expressed in terms of them, so one doesn't need to explicitly build the hadronic tensor in order to compute the cross section.

4.4.2 Born-only model and symmetry constraints

The most basic isobar model includes only the Born diagrams: this gives rise to the following current [14]

$$\begin{aligned}\widehat{J}^{\mu} = ieg_{K\Lambda N}\Bigg[&\gamma^5\frac{\not{p}+\not{q}+m_p}{s-m_p^2}\left(\gamma^{\mu}F_1^p + i\sigma^{\mu\nu}q_{\nu}\frac{\kappa_p}{2m_p}F_2^p\right) - \gamma^5\frac{q^{\mu}}{q^2}F_1^p \\ &+i\sigma^{\mu\nu}q_{\nu}\frac{\kappa_{\Lambda}}{2m_{\Lambda}}F_2^{\Lambda}\frac{\not{p}_2'-\not{q}+m_{\Lambda}}{u-m_{\Lambda}^2}\gamma^5 + \gamma^5\left(\frac{2p_1'^{\mu}-q^{\mu}}{t-m_K^2}+\frac{q^{\mu}}{q^2}\right)F^K\Bigg] \\ + ieg_{K\Sigma N}\, i\sigma^{\mu\nu}q_{\nu}&\frac{\kappa_{\Lambda\Sigma}}{m_{\Lambda}+m_{\Sigma}}F_2^{\Lambda\Sigma}\frac{\not{p}_2'-\not{q}+m_{\Sigma}}{u-m_{\Sigma}^2}\gamma^5,\end{aligned} \tag{4.26}$$

with the convention $\sigma^{\mu\nu} = \frac{i}{2}[\gamma^{\mu},\gamma^{\nu}]$. F_1 and F_2 are the Dirac and Pauli form factors, F^K is the kaon form factor and $F_2^{\Lambda\Sigma}$ is the $\Lambda\Sigma$ transition form factor. Here we have used a pseudo-scalar coupling, thus the contact diagram is not needed. For the pseudo-vector case, one needs to replace the $g_{K\Lambda N}\gamma^5$ vertex with the $g^{\text{pv}}_{K\Lambda N}\gamma^5\not{p}_1'$ vertex, where $g^{\text{pv}}_{K\Lambda N}$ and $g_{K\Lambda N}$ are related by $g_{K\Lambda N} = (m_p+m_{\Lambda})g^{\text{pv}}_{K\Lambda N}$. In order to preserve gauge invariance, one needs to add the contact diagram, whose Feynman rule is

$$ieg_{K\Lambda N}\frac{F_c}{m_p+m_{\Lambda}}\gamma^5\left(\not{q}\frac{q^{\mu}}{q^2}-\gamma^{\mu}\right), \tag{4.27}$$

where F_c is the contact form factor. The ambiguity between pseudo-scalar and pseudo-vector coupling hasn't been clearly resolved, but the community is leaning towards the pseudo-scalar theory, since it is simpler and can reproduce experimental data as satisfactorily as the pseudo-vector one. Additionally, an analysis has been performed near threshold for a mixture between pseudo-scalar and pseudo-vector theory, where it was seen that the fit to experimental data required a coupling that was mainly pseudo-scalar [16].

Another comment that can be made from the Born terms only is about the coupling constants. These are related to the pion-nucleon coupling constants by the $SU(3)_F$ symmetry, which allows to connect the couplings of the up-down sector to those of the strange sector. The relations are

$$g_{K\Lambda N} = -\frac{1}{\sqrt{3}}\left(3-2\alpha_D\right)g_{\pi NN}, \tag{4.28a}$$

$$g_{K\Sigma N} = \left(2\alpha_D-1\right)g_{\pi NN}, \tag{4.28b}$$

where $g_{\pi NN}$ is the pion-nucleon coupling constant, whose experimental value is given by $g_{\pi NN}^2/4\pi = 14.4$, and α_D is the fraction of the symmetric coupling in the πNN vertex, whose experimental value is 0.644 ± 0.006. However, due to the different mass of the strange quark with respect to the up and down quarks, $SU(3)_F$ is not exact, and the mass of the Λ is different from the mass of the proton. Since the breaking is of about

20%, we can give the following boundaries for $g_{K\Lambda N}$ and $g_{K\Sigma N}$, which can be used as constraints in the fitting procedure:

$$-4.4 \leq \frac{g_{K\Lambda N}}{\sqrt{4\pi}} \leq -3.0, \tag{4.29a}$$

$$0.8 \leq \frac{g_{K\Sigma N}}{\sqrt{4\pi}} \leq 1.3. \tag{4.29b}$$

An additional constraint that can be used when constructing isobar models is crossing symmetry, i.e. requiring that the same amplitude describes the $K^- + p \to \gamma + \Lambda$ process.

4.4.3 The inclusion of resonances

It turns out that the Born terms are not enough to describe the elementary process of kaon production, since the χ^2 from fits is rather large and the Λ polarization cannot be explained by Born therms alone. Since the threshold energy ($\sqrt{s} = 1610$ MeV) is higher than the rest masses of some baryon resonances, the contribution of excited states in all channels cannot be excluded, and thus one needs to include resonances in the current. Poles corresponding to the resonances are shifted to the complex plane, and the Feynman propagator is

$$\frac{1}{\not{q}_R - m_R + i\Gamma_R/2} = \frac{\not{q}_R + m_R - i\Gamma_R/2}{q_R^2 - m_R^2 + im_R\Gamma_R + \Gamma_R^2/4} \approx \frac{\not{q}_R + m_R - i\Gamma_R/2}{q_R^2 - m_R^2 + im_R\Gamma_R}, \tag{4.30}$$

where m_R and Γ_R refer to the mass and width of the resonance, respectively, and q_R is the exchanged momentum; the last equality refers to an approximation that is often used. In order to approximately account for unitarity corrections, one can also use energy-dependent widths. A problem that is faced when introducing resonances with spin $\geq \frac{3}{2}$ is that their Rarita-Schwinger description includes non-physical degrees of freedom, which may participate in the interaction if the particle is off-shell. A consistent prescription for the interaction of spin $\frac{3}{2}$ resonances was proposed by Pascalutsa [22] and was generalized to arbitrary spins by the Ghent group [23].

One of the characteristic features of isobar models for describing the electromagnetic production of kaons is the excessively large contribution of Born terms to the cross section, which overpredicts experimental data. Two main ways have been identified for reducing the strength of these contributions: introducing hadron form factors in the strong vertices, or exchanging hyperon resonances; different models can choose to adopt one or a combination of both solutions. Note that there is still an ambiguity for the selection of hadron form factors, which can be taken in any of the following forms

(dipole, multi-dipole, Gaussian and multi-dipole Gaussian, respectively):

$$\begin{aligned} F_d &= \frac{\Lambda_R^4}{\left(x - m_R^2\right)^2 + \Lambda_R^4} \\ F_{md} &= F_d^{J_R+1/2}\left(x, m_R, \Lambda_R\right) \\ F_G &= \exp\left[-\left(x - m_R^2\right)^2 / \Lambda_R^4\right] \\ F_{mdG} &= F_d^{J_R-1/2}\left(x, m_R, m_R\tilde{\Gamma}_R\right) F_G\left(x, m_R, \Lambda_R\right), \end{aligned} \tag{4.31}$$

where $x = s, t, u$ (according to the channel under consideration), J_R is the resonance spin, Λ_R is an energy cutoff parameter and $\tilde{\Gamma}_R$ is a modified width, namely

$$\tilde{\Gamma}_R = \frac{\Gamma_R}{\sqrt{2^{J_R/2} - 1}}. \tag{4.32}$$

Moreover, introducing hadron form factors breaks gauge invariance, which has to be restored via a contact interaction. Prescriptions for this contact interaction have been proposed by Ohta [24] and Haberzettl [25], the latter being the most commonly used due to its flexibility.

4.4.4 Variants of isobar models

Since there is no dominant resonance in the electromagnetic production of kaons, there are many existing isobar models, differing in the choice of resonant contributions and in values of coupling constants, that fit the experimental data equally well.

The first of these models to be developed is the Lyon-Saclay model, which includes the K^* and $K1$ resonances in the t-channel, three nucleon resonances in the s-channel and four hyperon resonances in the u-channel; it includes no hadron form factors and is constrained by $SU(3)_F$ and crossing symmetries. This group also performed an extensive analysis of different models including various combinations of hyperon resonances, and chose the one that fulfilled precise χ^2 requirements on various observables.

Another popular model is the Kaon-MAID one, which differs from the Lyon-Saclay model for the use of four nucleon resonances and no hyperon resonances; it uses dipole hadron form factors and energy-dependent widths, and is only constrained by $SU(3)_F$ symmetry. One of the nucleon resonances of this model was unobserved and absent from the initial fit, but it was predicted by the authors due to the fact that it could reproduce a particular resonant structure in the cross section data [26].

The last model we are going to see is the Ghent model. This group has tested various ways of suppressing the Born background, i.e. hyperon resonances only, hyperon

resonances and hadron form factors, and releasing the $SU(3)_F$ constraints to obtain smaller Born couplings. This model includes the same nucleon resonances as the Kaon-MAID, plus two hyperon resonances.

4.4.5 The Kaon-MAID model

Before moving on to the next section, let us provide some more detailed information about the Kaon-MAID model, since it is the one that we will use for our numeric calculations.

This parametrization consists of gauge invariant background and resonance terms [26]. The background terms include the standard s-, u-, and t-channel contributions, i.e. the proton, Λ, K^+, K^* and $K1$, along with a contact term, which is required to restore gauge invariance after the inclusion of hadron form factors. The resonant part consists of three nucleon resonances that have been found in coupled-channels analyses to have significant decay widths into the $K^+\Lambda$ channel: the $S_{11}(1650)$, $P_{11}(1710)$, and $P_{13}(1720)$. Additionally, the model includes the $D_{13}(1895)$ state, which is found to be important in the description of experimental data. Indeed, the parametrization was fitted to photoproduction total cross section data collected by SAPHIR [29]: as it can be seen in Fig. 4.2, the model cannot reproduce the resonant structure around a center of mass energy $W = 1900\,\mathrm{MeV}$ without the inclusion of this last resonance with a mass, width and coupling parameters that are in good agreement with the values predicted by quark model calculations [28]. Note that a number of fits with several states predicted by the quark model were performed in this energy region, allowing the fit to determine the mass, width and coupling constants of the resonances. While all of the examined resonances could reproduce the cross section structure and reduced the χ^2 value, only the $D_{13}(1895)$ state was predicted to also have significant photocouplings. However, the reproduction of the visual peak in the cross section data should not be interpreted as a steadfast evidence for the occurence of the $D_{13}(1895)$ missing resonance.

Since the amplitude of the Kaon-MAID model is not unitary by construction, energy-dependent widths along with partial branching fractions in the resonance propagators are included, which approximately account for unitarity corrections at tree-level. In order to regularize too large a contribution of Born terms, hadron form factors are implemented using the gauge method of Haberzettl [25]. This leads to a strong suppression of the electric part of the s-channel Born term, which results in a bump in the cross section prediction for small kaon angles (30°) and total energy higher than 1900 MeV. The fit to the data was significantly improved by allowing for separate cutoffs for the background

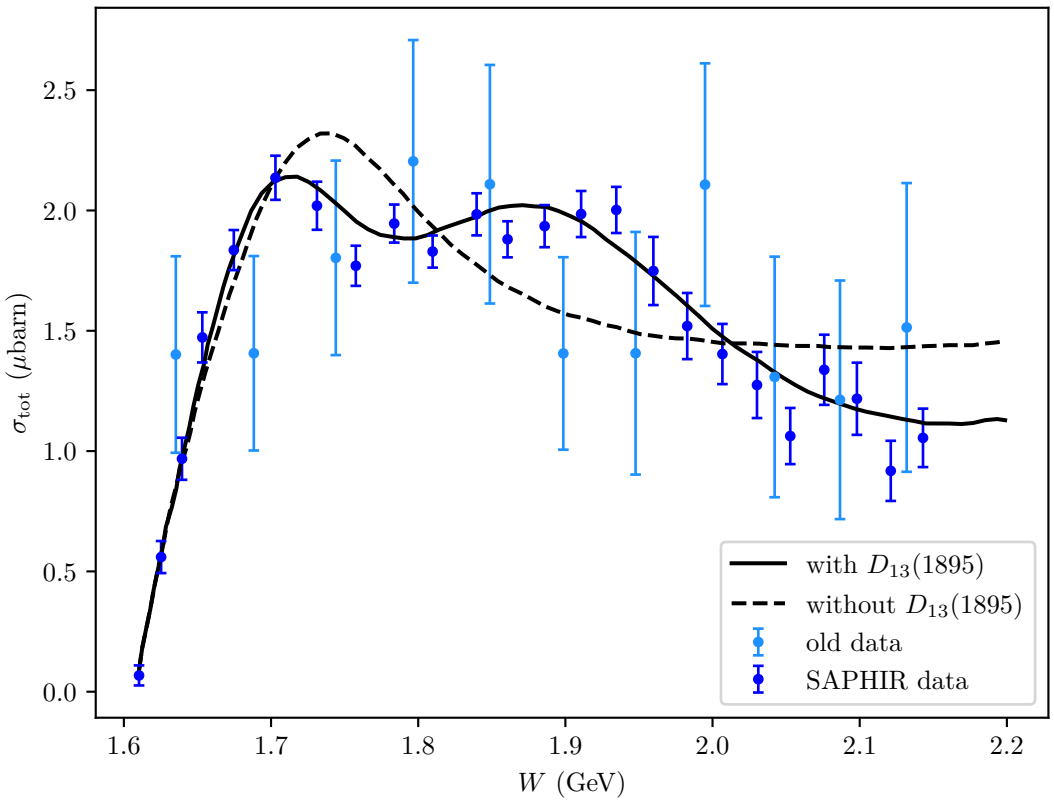

Figure 4.2: Total cross section for the elementary photoproduction process as a function of the total center of mass energy W. The solid line shows the prediction of the Kaon-MAID model, while the dashed line corresponds to the same model without the $D_{13}(1895)$ nucleon resonance. Blue data points are from the SAPHIR collaboration [29], and light blue points correspond to older data, for which references can be found in [29]. This plot is from [26].

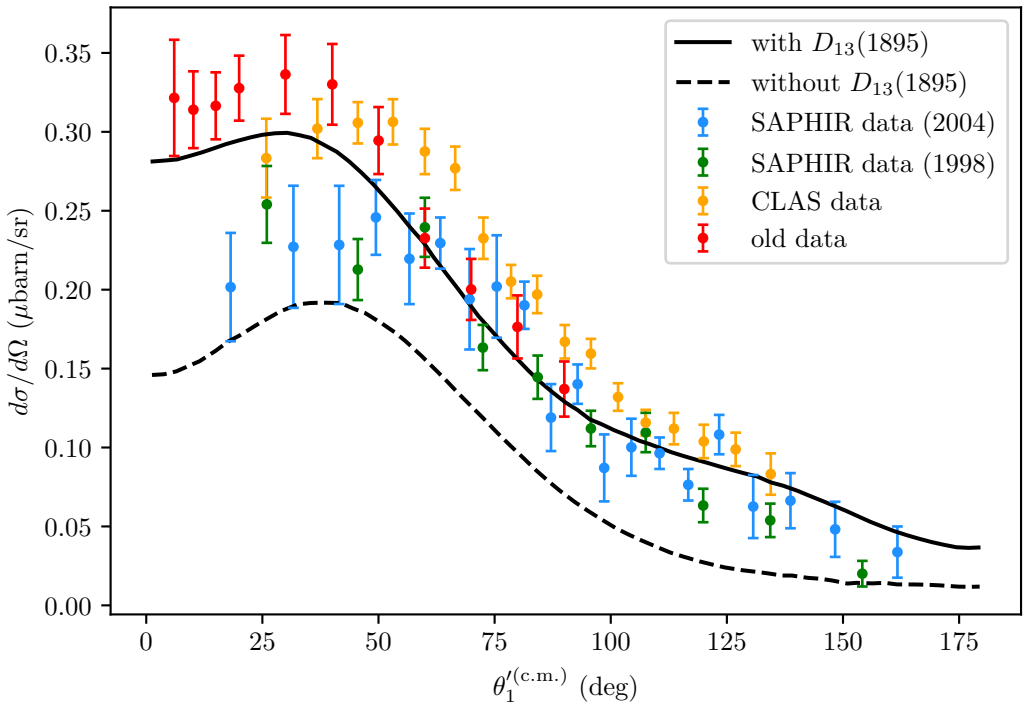

Figure 4.3: Differential cross section for the elementary photoproduction process as a function of the kaon center of mass angle, at a total energy $W = 1.835\,\mathrm{GeV}$. The solid line shows the prediction of the Kaon-MAID model, while the dashed line corresponds to the same model without the $D_{13}(1895)$ nucleon resonance. Blue points are from recent SAPHIR data [30], green points are from older SAPHIR data [29], yellow points are from the CLAS collaboration [31], and red points correspond to older data, for which references can be found in [29]. This plot is from [4].

and resonant sector form factors. For the former, the fits produce a soft value around 800 MeV, leading to a strong suppression of the background terms, while the resonant cutoff is determined to be 1900 MeV.

Fig. 4.3 shows more recent differential cross section data compared with Kaon-MAID predictions. Clearly there are some discrepancies among the experimental data (especially between the new SAPHIR [30] and CLAS [31] data), which have been thoroughly investigated in [34] with a multipole model. Anyway, this Figure shows that Kaon-MAID still gives reliable predictions for kaon photoproduction.

Finally, since this model was proposed in the energy range from threshold up to 2.2 GeV, the cross sections tend to become unreliable beyond this energy region.

A computational interface for this model is also available at [27].

4.4.6 Limitations of isobar models

The major drawback of isobar models is their limited scope in energy. Indeed, a realistic cross section should not increase with energy faster than $\ln^2(s/s_0)$, where s_0 is a reference scale which is commonly fixed to $1\,\mathrm{GeV}^2$ (this is the Froissart bound for unitarity [32]). On the contrary, in isobar models the contribution of the background rises as positive powers of s; up to a certain energy, this behavior can be compensated by the introduction of resonances that produce a destructive interference, but beyond 2 to 3 GeV, where introducing individual resonances no longer makes sense, unphysical, diverging behaviors appear. Thus, the validity of most isobar models is limited to the few-GeV region.

4.5 Regge-plus-resonance models

4.5.1 The Regge approach

The Regge phenomenology is a high-energy approach that was developed in order to overcome the energy limitations of isobar models. The starting point of this formalism is to consider partial wave amplitudes as a function of a complex angular momentum; poles of the amplitudes in the complex momentum plane are thought to correspond to resonant states, which can be classified into different families. These families are called Regge trajectories, and its members share the same quantum numbers. This allows us to treat the high-energy area, since here individual resonances can no longer be distinguished and the exchange of entire Regge trajectories dominates, instead.

In its simplest form, a Regge model is constructed starting from the Feynman amplitude for a given particle exchange and substituting the Feynman propagator with the Regge propagator $\mathcal{P}_{\mathrm{Regge}}$, a procedure known as "reggeization": this introduces the exchange of the entire Regge trajectory [1]. For $K\Lambda$ production, only the contributions of K and K^* are reggeized; this choice is motivated by the fact that the cross section is peaked at small values of $|t|$, which indicates the dominant role played by t-channel exchanges. However, the t-channel alone is not gauge invariant, so one also needs to include the electric part of the s-channel to restore it. The resulting amplitude reads

$$\mathcal{M}_{\mathrm{Regge}} = \mathcal{M}^{K}_{\mathrm{Regge}} + \mathcal{M}^{K^*}_{\mathrm{Regge}} + \mathcal{M}^{p,el}_{\mathrm{Feyn}} \cdot \mathcal{P}^{K}_{\mathrm{Regge}} \cdot \left(t - m_K^2\right). \tag{4.33}$$

[1] For a more detailed description of Regge propagators and trajectories, see Appendix B of [17].

This amplitude can then be written as in Eq. (4.24) and the Lorentz invariant amplitudes can be extracted.

Regge models have the benefit of including a relatively small numbers of free parameters, but data at high energies to fit them to is still scarce. They work especially well in the limit of extreme forward scattering angles for the kaon, corresponding to small $|t|$.

4.5.2 The Regge-plus-resonance approach

The purely non-resonant Regge description cannot reproduce the behavior of observables in the resonant region at lower energies, where peaks corresponding to individual resonances can be distinguished. In order to achieve a treatment that is valid at both low and high energies, one can extend the reggeized background with a small number of resonant diagrams in the s-channel. For these diagrams, the standard Feynman propagator is used; moreover, since resonances aren't expected to contribute to observables at high energies, one needs to introduce hadron form factors that limit their contribution to the resonant region and ensure a smooth transition to the high-energy region. The amplitude that is constructed with this procedure reads

$$\mathcal{M} = \mathcal{M}_{\text{Regge}} + \mathcal{M}_{\text{reson}}. \tag{4.34}$$

This approach is known as Regge-plus-resonance (RPR).

RPR models have the benefit of being able to reproduce low- and high-energy data (they have been shown to be valid up to $E_\gamma^{\text{lab}} \approx 16$ GeV), and also of introducing only 3 free parameters to model the non-resonant background. Another feature of these models is that, contrary to isobar models, the Born contribution doesn't turn out to be too strong, so hadron form factors are not needed for background terms.

There are several variants of RPR models, which mainly differ by the combination of nucleon resonances they include. They were analyzed by De Cruz *at al.* [33], and two best models were identified, the first one containing 8 resonances and the second one containing 5.

4.5.3 Hybrid isobar - Regge approach

Another option to get the high-energy behavior of a Regge model and keep the resonant behavior at low energies is to build a hybrid between an isobar and a Regge model. This has been done, e.g., in [19]: for energies below $\sqrt{s_1} = 2\,\text{GeV}$, the invariant amplitudes A_i are given by an isobar model, and for energies above $\sqrt{s_2} = 3\,\text{GeV}$ they are given by

a Regge model. In the transition region, the two types of amplitudes are combined as

$$A_i^{\text{trans}} = \frac{1}{s_1 - s_2}\left((s - s_2)\, A_i^{\text{isobar}} + (s_1 - s)\, A_i^{\text{Regge}}\right). \tag{4.35}$$

4.6 Multipoles models

The multipoles framework introduces a different way to model the background and the resonant part separately. This approach deals directly with the electric and magnetic photon couplings, and the resonance terms are parameterized with a Breit-Wigner form

$$A_{\ell\pm}^R(W) = \bar{A}_{\ell\pm}^R c_{KY} \frac{f_{\gamma R}(W)\Gamma_{\text{tot}}(W) M_R f_{KR}(W)}{M_R^2 - W^2 - iM_R\Gamma_{\text{tot}}(W)} e^{i\phi}. \tag{4.36}$$

Here, $W = \sqrt{s}$ is the total center of mass energy, c_{KY} is the isospin factor, which has a value of -1, f_{KR} is the Breit-Wigner factor indicating the strength of the decay of a resonance R with a physical mass M_R and a total width $\Gamma_{\text{tot}}(W)$, $f_{\gamma R}$ represents the γNR vertex, and ϕ is the corresponding phase [2]. The background is modeled with an arbitrary, smooth function. This is usually built from Feynman diagrams, which include the Born s-, t- and u-channels plus the K^* and $K1$ exchange in the t-channel; hadron form factors are introduced in the strong vertices in order to avoid diverging behaviors at large energies. This kind of background is gauge invariant and crossing symmetric. The observables predicted by these theories are then computed from CGLN amplitudes, which contain linear combinations of the $A_{\ell\pm}$ in addition to the background originating from Feynman diagrams.

These models have the benefit of easily allowing to include a large number of resonances with arbitrarily large spins, since each resonance only contributes with a term of the form (4.36), whereas isobar models require a more cumbersome treatment through Feynman diagrams. The electric and magnetic photon couplings can also be directly related to the helicity amplitudes $A_{1/2}$ and $A_{3/2}$ [3] listed in the Particle Data Group review [35].

[2] For additional details on the mathematical form of these factors, see Section II.B of [34]

[3] See, e.g., Table I of [34]

Chapter 5

Numerical analysis

5.1 The Python program

In order to quantitatively evaluate the triple differential cross section for a $e + A \to e' + K^+ + {}_\Lambda A$ reaction (Eq. (3.8)) with unpolarized electron beams, we have developed a Python program that performs numerical computations for a specified nuclear target and fixed kinematical conditions. The program consists of four modules, for each of which we present a flowchart (Fig.s 5.1, 5.3, 5.4 and 5.5).

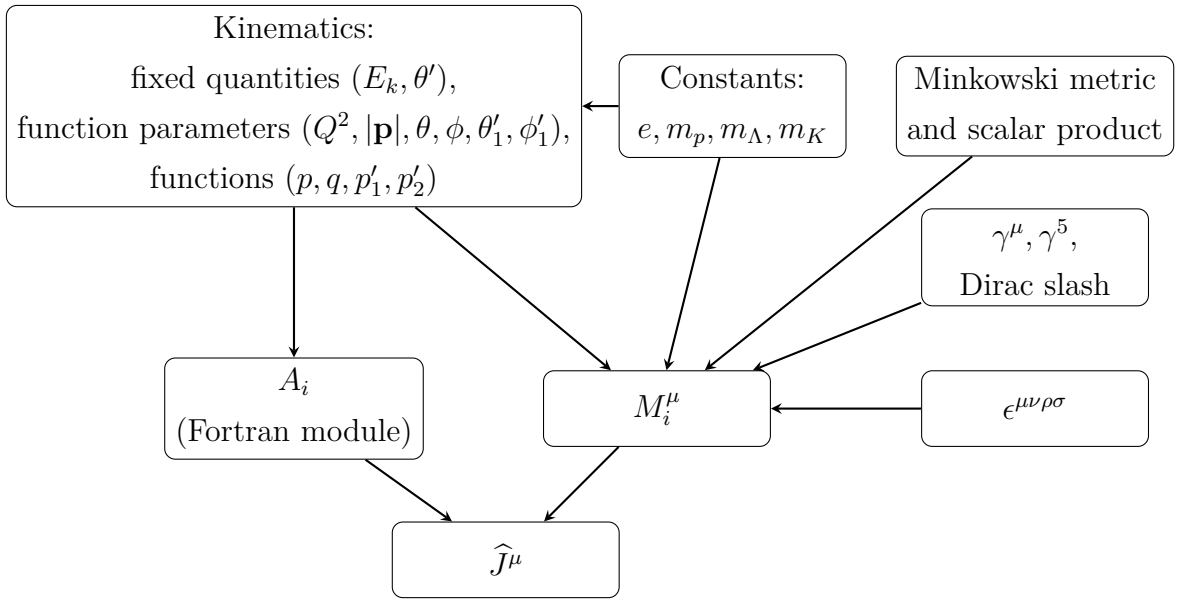

Figure 5.1: Flowchart for the first module of the Python program, dealing with the elementary process.

The first module deals with the elementary process $e + p \to e' + K + \Lambda$. As shown in Fig. 5.1, it contains functions to determine the four-momenta of all the particles

involved, given some initial conditions. It also contains the routine for the evaluation of the elementary operator $\widehat{J}^\mu$ as a function of the four-momenta of the virtual photon, proton, kaon and Λ. $\widehat{J}^\mu$ is computed as in Eq. (4.24), where the gauge invariant matrices M_i are evaluated through Eq. (4.25), while the Lorentz invariant amplitudes A_i are those of the Kaon-MAID model. The Kaon-MAID parametrization has been kindly provided to us by T. Mart by means of a Fortran module, which has been integrated into the Python program.

In order to test the correct implementation of the elementary operator, which is crucial for the evaluation of the full nuclear operator, we have used it to compute the elementary electroproduction cross section in the center of mass frame. The transverse and longitudinal differential cross sections can be evaluated using the following formulae [3]:

$$\frac{d\sigma_T}{d\Omega_1'} = \frac{|\mathbf{p}_1'|\sqrt{s}}{2\left(s-m_p^2\right)}\left(\tilde{W}^{11}+\tilde{W}^{22}\right), \tag{5.1a}$$

$$\frac{d\sigma_L}{d\Omega_1'} = \frac{|\mathbf{p}_1'|\sqrt{s}}{2\left(s-m_p^2\right)}\frac{2E_{p_1'}E_{p_2'}Q^2}{\omega^2 s}\tilde{W}^{33}. \tag{5.1b}$$

Here, $\tilde{W}^{\mu\nu}$ is the hadronic tensor for the elementary reaction, defined as

$$\begin{aligned}\tilde{W}^{\mu\nu} &= \sum_{s_p,s_\Lambda=\pm\frac{1}{2}}\left(\overline{u}(\mathbf{p}_2',s_\Lambda)\widehat{J}^\mu u(\mathbf{p},s_p)\right)\left(\overline{u}(\mathbf{p}_2',s_\Lambda)\widehat{J}^\nu u(\mathbf{p},s_p)\right)^* = \\ &= \sum_{i,j=1}^{6} A_i A_j^*\, tr\left[M_i^\mu(\not{p}+m_p)\overline{M_j^\nu}(\not{p}_2'+m_\Lambda)\right],\end{aligned} \tag{5.2}$$

where $u(\mathbf{p},s_p)$ and $u(\mathbf{p}_2',s_\Lambda)$ are free Dirac spinors for the proton and Λ, respectively, while $\overline{M_i^\mu} \equiv \gamma^0 M_i^{\mu\dagger}\gamma^0$: it can be easily checked that

$$\begin{aligned}\overline{M_1^\mu} &= M_1^\mu, & \overline{M_4^\mu} &= -M_4^\mu,\\ \overline{M_2^\mu} &= -M_2^\mu, & \overline{M_5^\mu} &= -M_5^\mu,\\ \overline{M_3^\mu} &= M_3^\mu, & \overline{M_6^\mu} &= M_6^\mu.\end{aligned} \tag{5.3}$$

The results of this calculation for a center of mass energy of $W = 1.84\,\mathrm{GeV}$ and a kaon angle $\theta_1'^{(\mathrm{c.m.})} = 0$ are shown in Fig. 5.2. We can see that our calculation is in very good agreement with the one from the Kaon-MAID interface [27], and it nicely compares with experimental data.

The second module simply contains a function that evaluates the momentum space transform of the $f(r)$ and $g(r)$ spinor wavefunctions that appear in Eq. (3.83), as shown in Fig. 5.3. The input is assumed to be evaluated on a lattice of radial values, and the

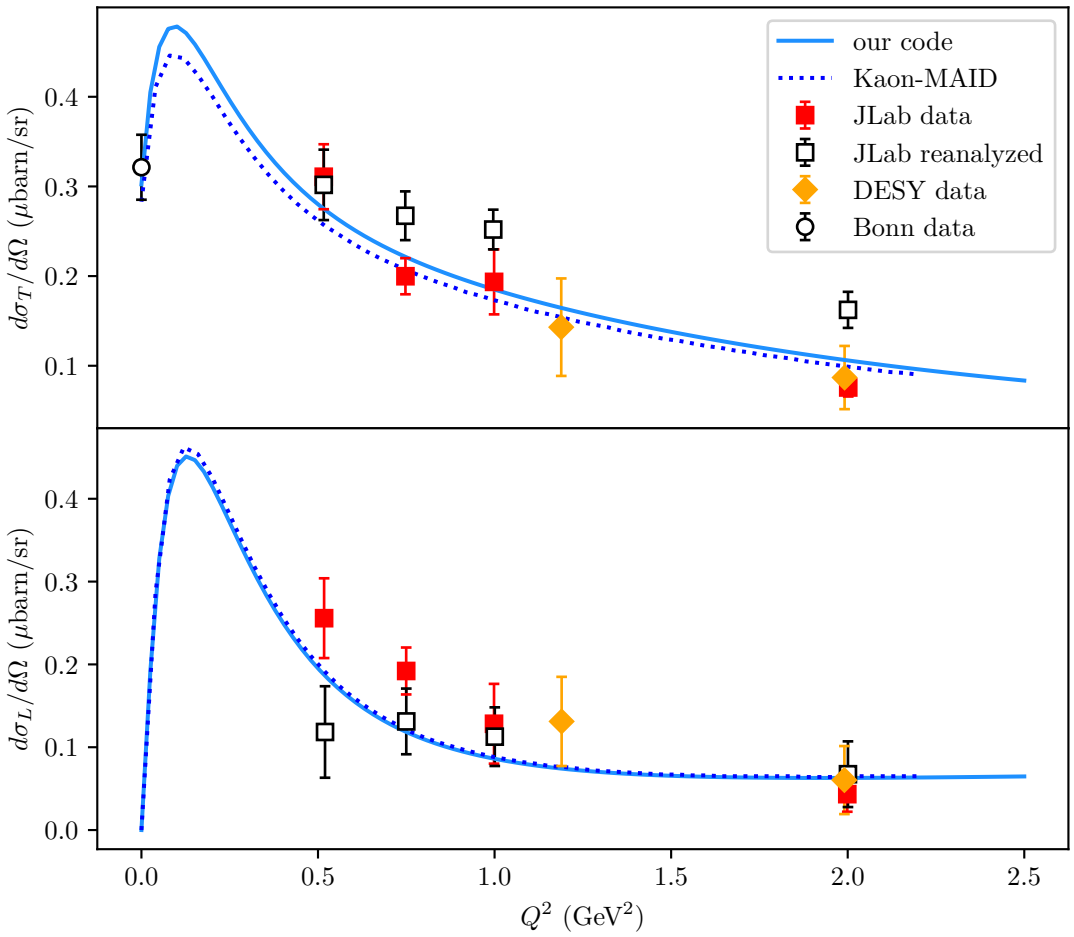

Figure 5.2: Transverse (above) and longitudinal (below) differential cross section for the elementary electroproduction process as a function of the photon virtuality Q^2, at a total energy $W = 1.84\,\mathrm{GeV}$ and kaon angle $\theta_1'^{(\mathrm{c.m.})} = 0$. The solid line shows the calculation with our code, while the dotted line shows the one from the Kaon-MAID interface [27]. Solid squares show JLab data [37], which have been reanalyzed by Mohring *et al.* [38], as shown by open squares; solid diamonds show SAPHIR data [39], while the open circle is a photoproduction point from Bonn data [40].

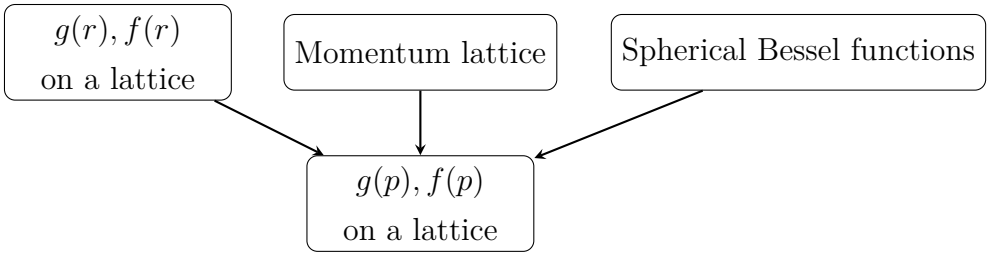

Figure 5.3: Flowchart for the second module of the Python program, dealing with the momentum space transform of the $g(r)$ and $f(r)$ wavefunctions.

output is given on a regular momentum lattice that can be adjusted as needed. Since we are operating with discretized functions, the integration is performed using a Simpson algorithm. The transformed wavefunctions are then written to files for later use.

The third and more involved module, whose flowchart can be found in Fig. 5.4, evaluates the components of the hadronic tensor $W^{\mu\nu}$ through the formula in (3.19), where the $w^{\mu}_{\alpha_A\alpha_Y}$ are given by Eq. (3.69). In our case, the quantum numbers α_A and α_Y that are summed over simply correspond to the total magnetic quantum numbers of the bound proton and Λ, i.e. m_p and m_Λ, respectively. In order to perform these calculations, this module also contains functions to build the bound spinor wavefunctions in momentum space using Eq. (3.83), where the $f(p)$ and $g(p)$ are read from the files which have been written with the previous module and interpolated for arbitrary momentum values. The most computationally demanding function is the one that evaluates the integral in Eq. (3.69), which repetitively calls the function which computes the integrand. The integration is done using a Monte Carlo method, since we have found it to be considerably faster than Gaussian approaches; more precisely, we use the *Vegas* routine developed by G. P. Lepage [41]. The correct use of this routine was initially checked by verifying the normalization of the bound spinor wavefunctions. The Monte Carlo fluctuations for the current code give rise to differential cross sections that are accurate up to the fourth significant digit. As for the integrand function, given a proton three-momentum in spherical coordinates, it first evaluates the momenta of the other particles involved in the $\gamma + p \to K + \Lambda$ process, also making use of other kinematical conditions that are provided as inputs, tanks to the elementary module; then it extracts the spherical coordinates of the Λ three-momentum and computes the sandwich $\overline{\mathcal{U}}_\Lambda \widehat{J}^\mu \mathcal{U}_p$.

The last module deals with the kinematics of a full nuclear reaction $e + A \to e' + K^+ + {}_\Lambda A$, then computes the matrix element using Eq. (3.15) and the triple differential cross section using Eq. (3.8), as can be seen in Fig. 5.5.

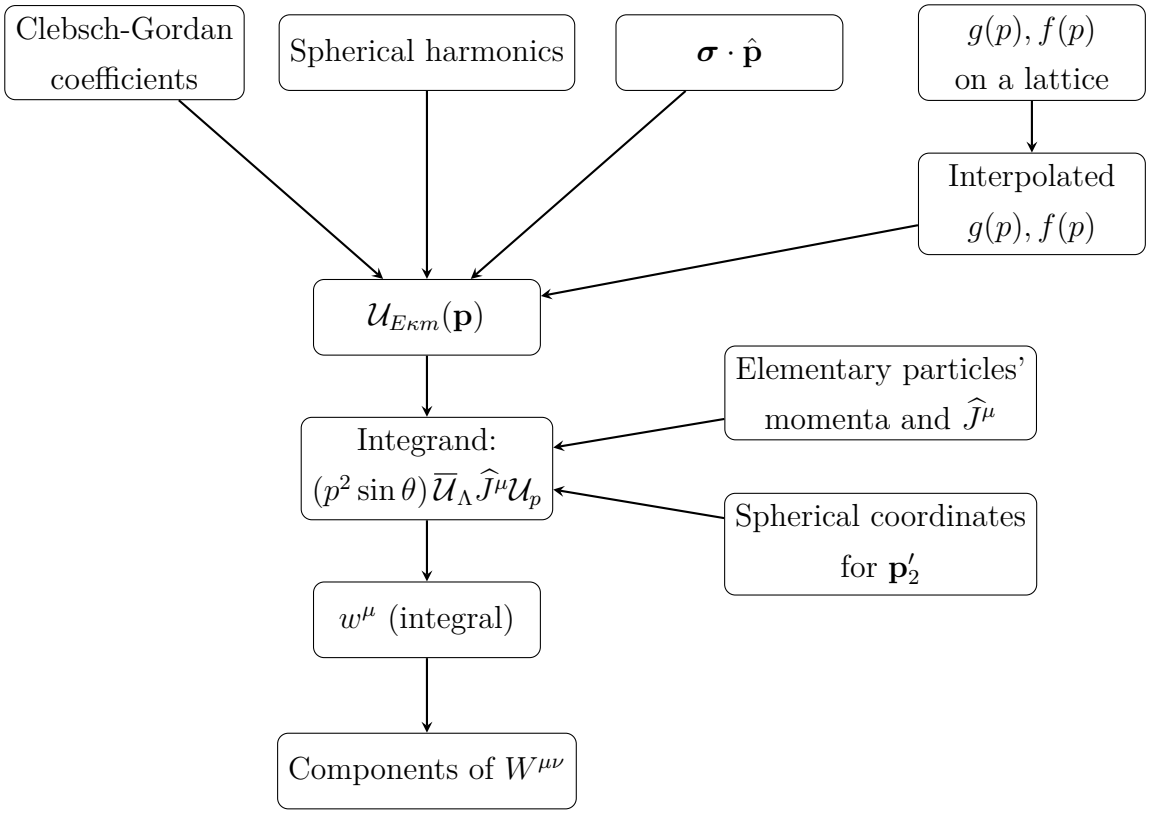

Figure 5.4: Flowchart for the third module of the Python program, dealing with the nuclear current and the hadronic tensor.

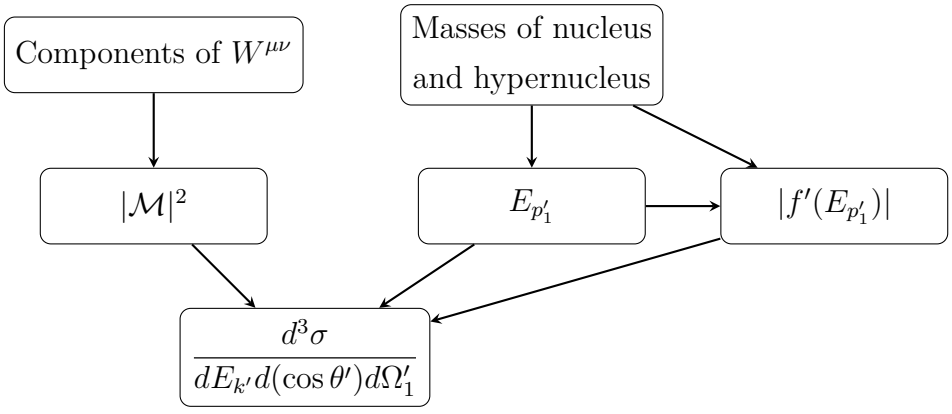

Figure 5.5: Flowchart for the fourth module of the Python program, dealing with the final stages of the computation of the triple differential cross section.

5.2 Ingredients for the $^{12}C(e,e'K)^{12}_{\Lambda}B$ calculation

The initial ingredients that are necessary to perform the differential cross section calculation are essentially the f and g wavefunctions of the bound proton and Λ and their binding energies for the orbitals they can belong to.

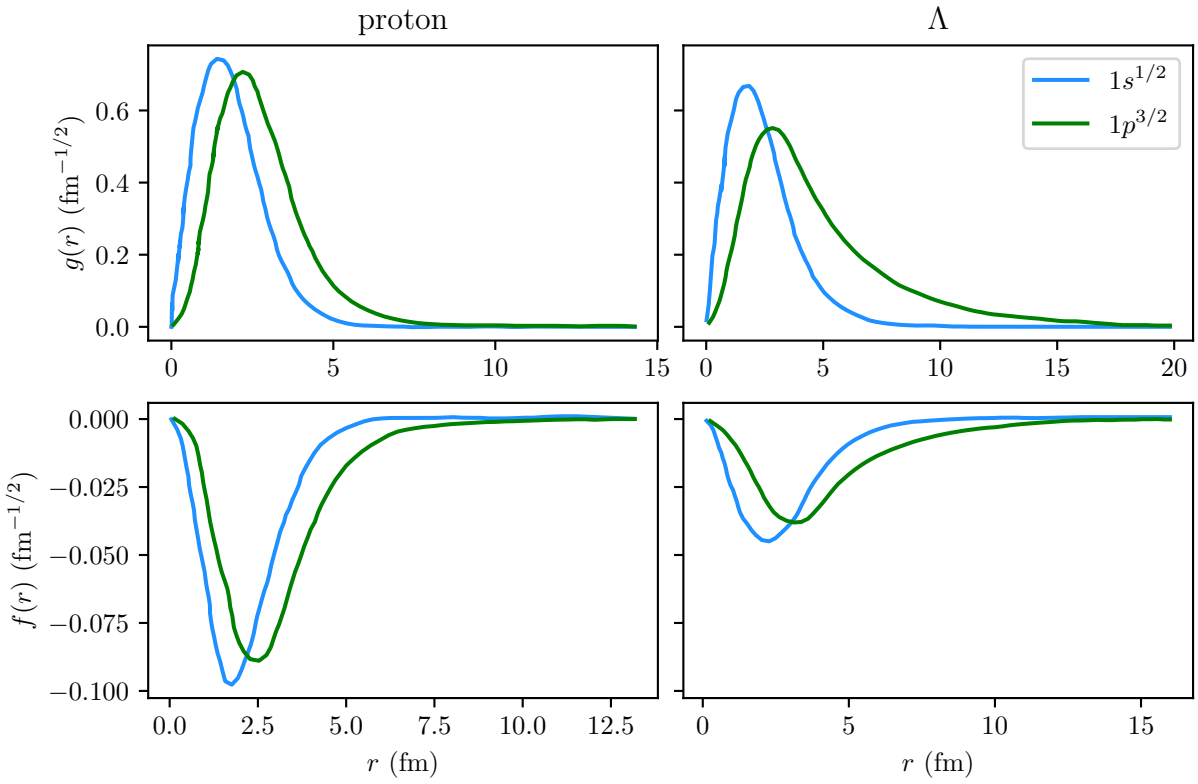

Figure 5.6: Wavefunctions in configuration space for the bound proton and Λ in two different orbitals of the ^{12}C nucleus and the $^{12}_{\Lambda}B$ hypernucleus, respectively. The upper panel shows the upper $g(r)$, while the lower panel shows the lower $f(r)$ of Eq. (3.70).

In Fig. 5.6 we plot the radial g and f functions, respectively, for the $1s^{1/2}$ and $1p^{3/2}$ orbitals for both the proton in the ^{12}C nucleus and the Λ in the $^{12}_{\Lambda}B$ hypernucleus. They are obtained from a relativistic mean field model, namely the FSUGold model [44]. In Fig. 5.7 we show the momentum space counterparts of Fig. 5.6, which have been obtained with the transformation module of our program.

The binding energies for the proton and Λ are listed in Table 5.1. The proton binding energies are an average of four different models, namely the QHDI [42], QHDII [42], NL3 [43] and FSUGold [44] models, while the Λ binding energies are only from the FSUGold model.

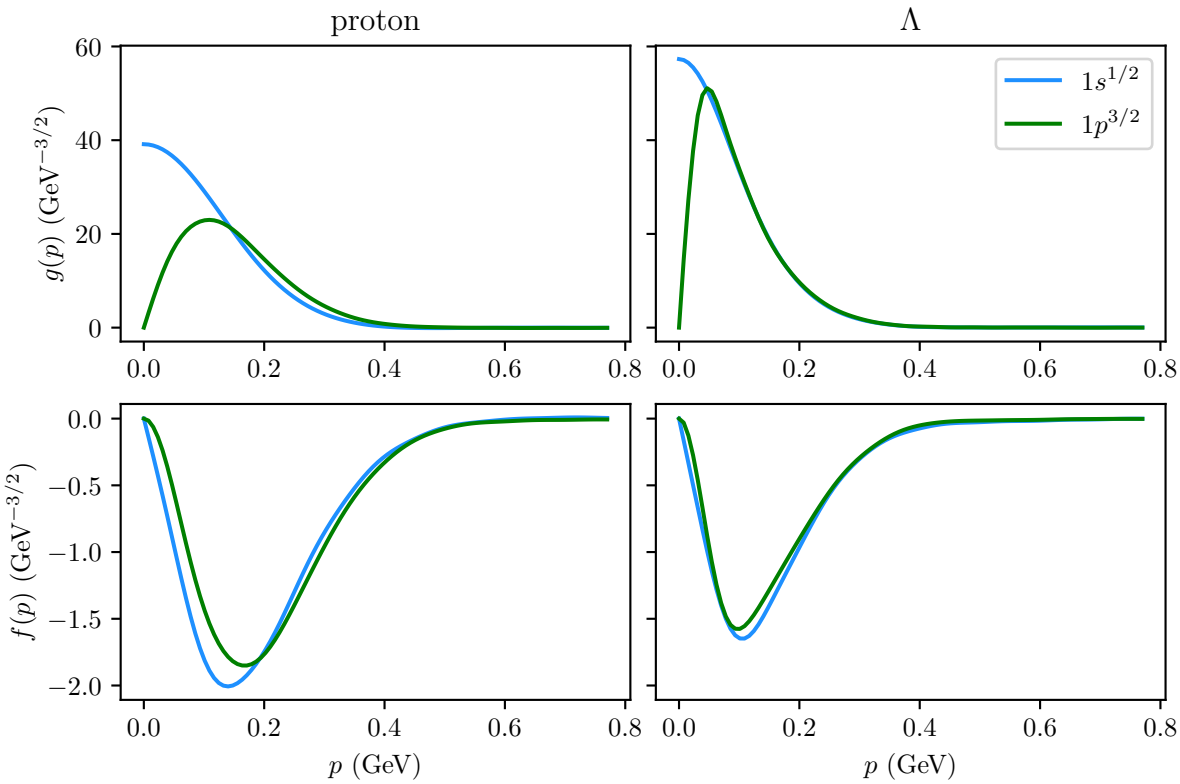

Figure 5.7: Wavefunctions in momentum space for the bound proton and Λ in two different orbitals of the ^{12}C nucleus and the $^{12}_{\Lambda}B$ hypernucleus, respectively. The upper panel shows the upper $g(p)$, while the lower panel shows the lower $f(p)$ of Eq. (3.83).

These binding energies give rise, through the formula

$$M_{_\Lambda A} = M_A - \left(m_p - E_B^{(p)}\right) + \left(m_\Lambda - E_B^{(\Lambda)}\right), \tag{5.4}$$

to the hypernucleus masses that are listed in Table 5.2.

5.3 $^{12}C(e,e'K)^{12}_{\Lambda}B$ calculation results

We have computed the triple differential cross section for the $^{12}C(e,e'K)^{12}_{\Lambda}B$ process as a function of the kaon polar angle in three different kinematical conditions, which are summarized in Table 5.3. For the first conditions, we have an incident electron energy of 3 GeV, an outgoing electron energy of 2 GeV, an electron scattering angle of 5° and a vanishing kaon azimuthal angle. These are the same conditions as the main calculation in [3], allowing us to check the correct implementation of our code. The results for

	$1s^{1/2}$	$1p^{3/2}$
$p\,(^{12}C)$	42.713 MeV	14.685 MeV
$\Lambda\,(^{12}_{\Lambda}B)$	1.11 MeV	12.31 MeV

Table 5.1: Binding energies for the proton and Λ in the $1s^{1/2}$ and $1p^{3/2}$ orbitals of ^{12}C and $^{12}_{\Lambda}B$, respectively.

	$\Lambda:\ 1s^{1/2}$	$\Lambda:\ 1p^{3/2}$
$p:\ 1s^{1/2}$	11.39694 GeV	11.38574 GeV
$p:\ 1p^{3/2}$	11.36891 GeV	11.35771 GeV

Table 5.2: Masses of the $^{12}_{\Lambda}B$ hypernucleus for different combinations of the Λ-particle, proton-hole orbitals.

this calculation are shown in Fig. 5.8. We can see that the curves for all the different combinations of orbitals have the same structure, namely they are larger at vanishing kaon angle and fall off when the kaon angle increases, reaching zero around 35°. The curves can be divided into two groups: the higher one for the proton hole in the $1p^{3/2}$ orbital and the lower one for the proton hole in the $1s^{1/2}$ orbital. In both groups, the larger cross section is obtained for the Λ in the $1p^{3/2}$ orbital. We can also see that our result is in rough agreement with the one in [3]: the shapes of the curves and their order of magnitude are very similar, and the differences are likely due to the use of different models for the elementary process.

For the next calculation we have kept the same conditions as before, except increasing the electron scattering angle to 10°, which increases the photon virtuality (see Eq. (3.36)). As we can see in Fig. 5.9, the structure of the four curves remains essentially the same, but the overall magnitude of the cross section decreases. This can be explained by the increase in photon virtuality, which corresponds to a higher momentum transfer.

Then, we have decreased the ingoing and outgoing electron energies to 2 and 0.8

E_k	$E_{k'}$	θ'	ϕ'_1	Q^2
3 GeV	2 GeV	5°	0	0.0456636229 GeV^2
3 GeV	2 GeV	10°	0	0.1823069639 GeV^2
2 GeV	0.8 GeV	5°	0	0.01217696611 GeV^2

Table 5.3: Different kinematical conditions that have been tested in Fig.s 5.8, 5.9 and 5.10.

GeV, respectively, while restoring the electron scattering angle to 5°. Fig. 5.10 shows that this leads to a slight decrease in the cross section; additionally, the gap between the two groups of curves increases, while the one between the two curves in the same group decreases.

Finally, we have computed the triple differential cross section as a function of Q^2 for an incident electron energy of 3 GeV, an electron scattering angle of 5° and kaon angles $(\theta_1', \phi_1') = (5°, 0°)$. Varying Q^2 corresponds to varying the final electron energy (see again Eq. (3.36)), as shown in the axes of Fig. 5.11. From this Figure we can see that the cross section is rather low at low final energies, then peaks around 1.6 GeV, has a secondary peak at 2 GeV and falls off when approaching the maximum energy permitted by the kinematics. The relative magnitude of the cross section for the different particle-hole combinations stays more or less the same, except around 2 GeV where the gap between curves differing by the Λ orbital increases; moreover, up to 1 GeV the cross section for the proton in the $1p^{3/2}$ and the Λ in the $1s^{1/2}$ orbital is slightly larger than the one for the proton in the $1p^{3/2}$ and the Λ in the $1p^{3/2}$ orbital, while for larger energies this behavior is inverted.

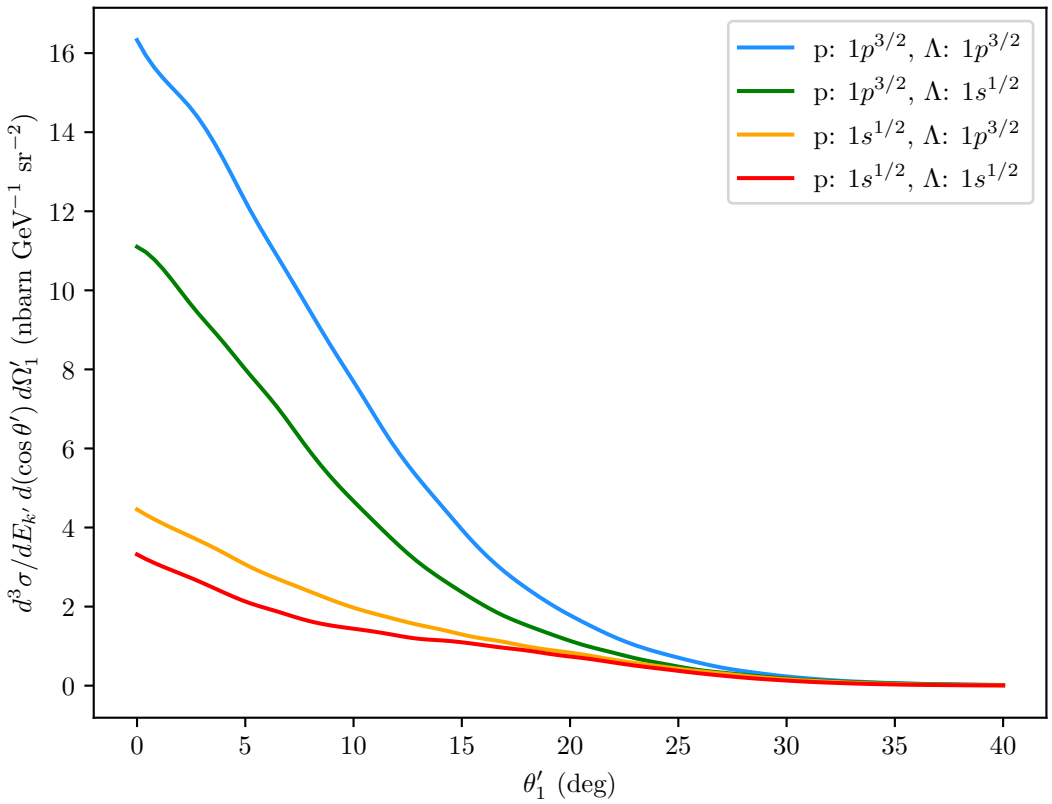

Figure 5.8: Triple differential cross section for the $e + {}^{12}C \to e' + K + {}^{12}_{\Lambda}B$ reaction, as a function of the kaon polar angle θ_1', for an ingoing electron energy $E_k = 3\,\text{GeV}$, an outgoing electron energy $E_{k'} = 2\,\text{GeV}$, an electron scattering angle $\theta' = 5°$ and a kaon azimuthal angle $\phi_1' = 0°$. This corresponds to a photon virtuality $Q^2 = 0.046\,\text{GeV}^2$. Different colors indicate different combinations of the proton-hole and Λ-particle orbitals.

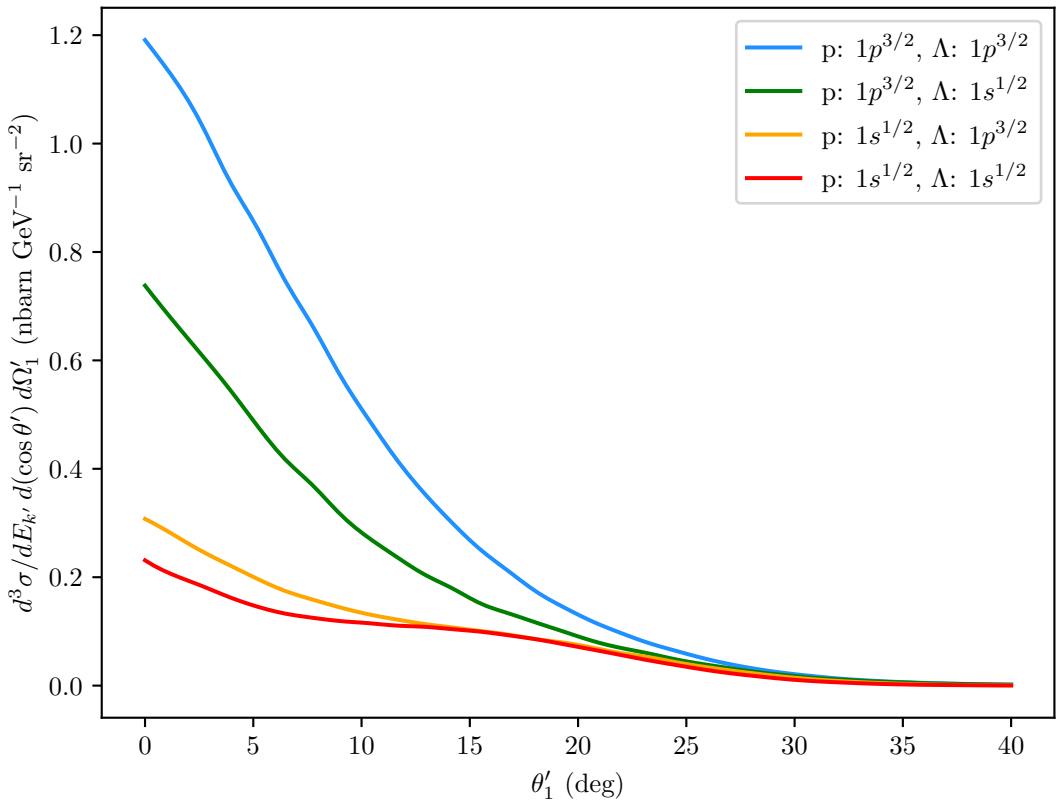

Figure 5.9: Triple differential cross section for the $e + {}^{12}C \to e' + K + {}^{12}_{\Lambda}B$ reaction, as a function of the kaon polar angle θ_1', for an ingoing electron energy $E_k = 3\,\text{GeV}$, an outgoing electron energy $E_{k'} = 2\,\text{GeV}$, an electron scattering angle $\theta' = 10°$ and a kaon azimuthal angle $\phi_1' = 0°$. This corresponds to a photon virtuality $Q^2 = 0.18\,\text{GeV}^2$. Different colors indicate different combinations of the proton-hole and Λ-particle orbitals.

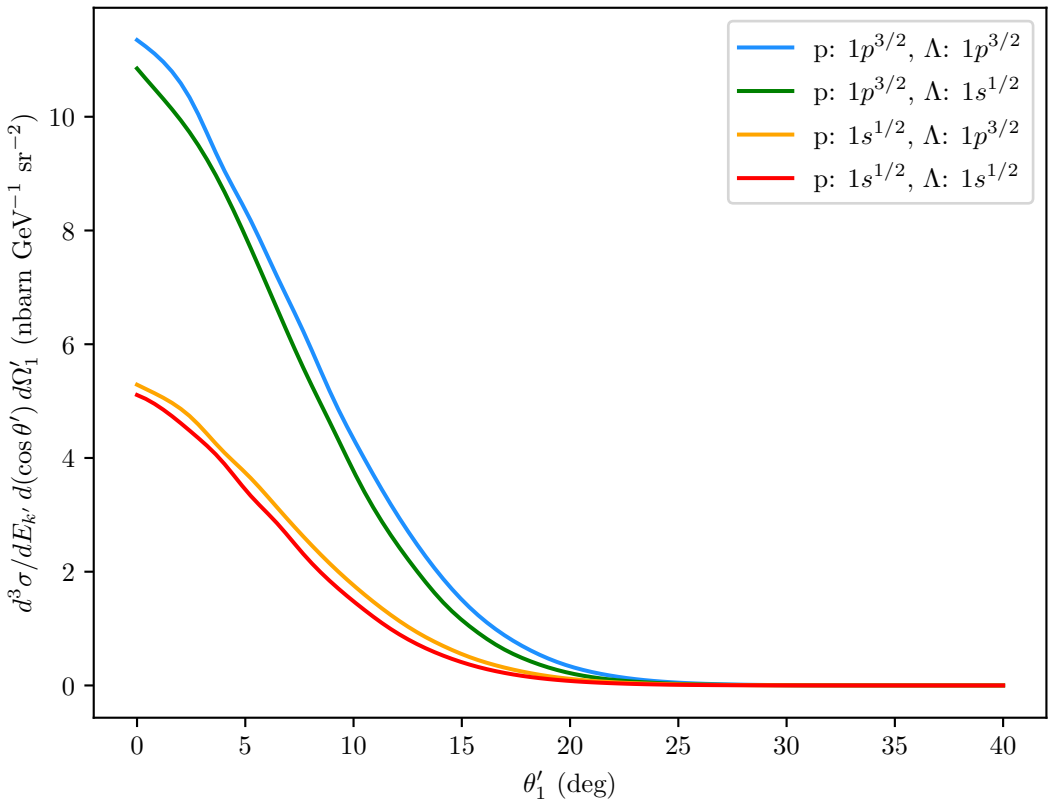

Figure 5.10: Triple differential cross section for the $e + {}^{12}C \to e' + K + {}^{12}_{\Lambda}B$ reaction, as a function of the kaon polar angle θ_1', for an ingoing electron energy $E_k = 2\,\text{GeV}$, an outgoing electron energy $E_{k'} = 0.8\,\text{GeV}$, an electron scattering angle $\theta' = 5°$ and a kaon azimuthal angle $\phi_1' = 0°$. This corresponds to a photon virtuality $Q^2 = 0.012\,\text{GeV}^2$. Different colors indicate different combinations of the proton-hole and Λ-particle orbitals.

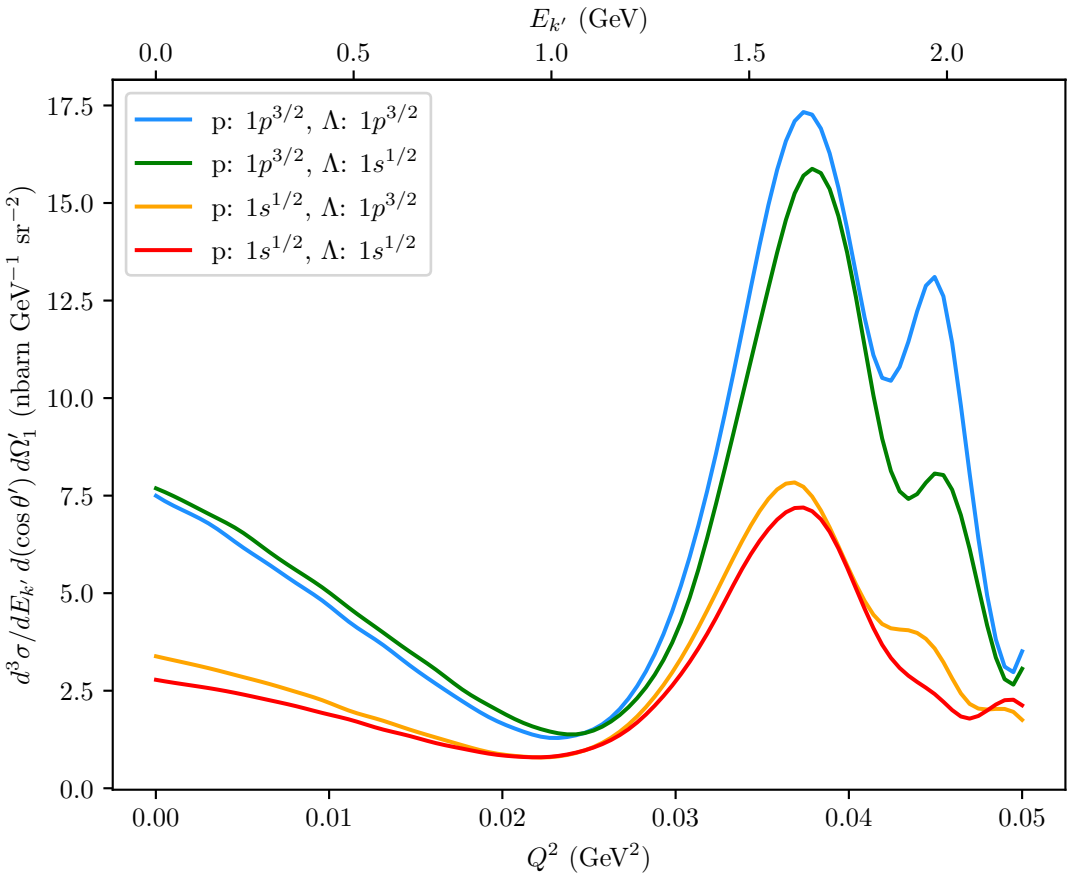

Figure 5.11: Triple differential cross section for the $e + {}^{12}C \to e' + K + {}^{12}_{\Lambda}B$ reaction, as a function of the photon virtuality Q^2, for an ingoing electron energy $E_k = 3\,\text{GeV}$, an electron scattering angle $\theta' = 5°$ and a kaon solid angle $(\theta_1', \phi_1') = (5°, 0°)$. The upper axis shows the values of outgoing electron energies $E_{k'}$ that correspond to the different values of Q^2. Different colors indicate different combinations of the proton-hole and Λ-particle orbitals.

Chapter 6

Conclusions and outlook

To summarize, we have seen that hypernuclear spectroscopy is an interesting field of study, because it allows us to gain insights on the ΛN and $\Lambda\Lambda$ interactions, which are expected to play an important role in dense nuclear matter like neutron stars. Experiments that use $(e, e'K)$ reaction to inspect different hypernuclei are receiving a lot of attention lately, and since a sound theoretical background is needed in order to understand experimental results, we have focused our attention on the numerical evaluation of differential cross sections for these reactions. We have developed the formalism for the computation of triple differential cross sections, particularly for totally unpolarized electron beams, using the impulse approximation. This approximation allows us to view the full nuclear reaction as the interaction of a virtual photon with a single proton in the target nucleus, while the other nucleons act as spectators. We have written the matrix element squared as a contraction of a leptonic and a hadronic tensor, and we have parametrized the hadronic tensor in a model-independent way which makes use of structure functions. Since a good knowledge of the elementary process $e+p \to e'+K+\Lambda$ is required to successfully describe this interaction, we also have reviewed the different approaches to model it. We have focused on hadrodynamical, single-channel approaches, which include isobar models, Regge-plus-resonance models and multipoles models.

We have then developed a Python program to numerically compute unpolarized triple differential cross sections, and we have presented our first results for computations on a ^{12}C target nucleus. We have used bound proton and Λ wavefunctions from the FSUGold model and the Kaon-MAID parametrization for the elementary current operator. Our results show that the triple differential cross section for the different particle-hole orbitals combinations has an order of magnitude of about $10\,\mathrm{nbarn\,GeV^{-1}sr^{-2}}$. The cross section is larger for the proton in the $1p^{3/2}$ orbital; all cross sections for different combinations of

particle-hole orbitals have the same structure, smoothly decreasing as a function of the kaon polar angle. We found this to be true for various kinematical conditions. Moreover, our results are in rough agreement with the ones presented by [3], the differences being attributable to a different parametrization of the elementary operator.

The work presented in this thesis has several possibilities for future extensions. First, the program can be used on many different nuclear reactions, including the promising ^{208}Pb, since we have the ability to compute nucleon wavefunctions from mean field and ab initio methods. Additionally, the cross section formula can be straightforwardly generalized to different polarizations of the electron beams.

Bibliography

[1] O. Hashimoto and H. Tamura, *Spectroscopy of Lambda hypernuclei*, Prog. Part. Nucl. Phys. **57** (2006), 564-653 doi:10.1016/j.ppnp.2005.07.001

[2] O. Benhar, *Extracting Hypernuclear Properties from the* $(e, e'K^+)$ *Cross Section*, [arXiv:2006.12084 [nucl-th]].

[3] B. I. S. van der Ventel, T. Mart, H. F. Lu, H. L. Yadav and G. C. Hillhouse, *Electromagnetic production of hypernuclei*, Annals Phys. **326** (2011), 1085-1106 doi:10.1016/j.aop.2011.02.003 [arXiv:1102.2699 [nucl-th]].

[4] T. Mart and B. I. S. van der Ventel, *Photo- and Electroproduction of the Hypertriton on He-3*, Phys. Rev. C **78** (2008), 014004 doi:10.1103/PhysRevC.78.014004 [arXiv:0806.4835 [nucl-th]].

[5] B. F. Gibson and E. V. Hungerford, *A Survey of hypernuclear physics*, Phys. Rept. **257** (1995), 349-388 doi:10.1016/0370-1573(94)00114-I

[6] J. Adam, J. Mares, O. Richter, M. Sotona and S. Frullani, *Electroproduction of strangeness*, Czech. J. Phys. **42** (1992), 1167-1196 doi:10.1007/BF01591400

[7] P. Bydžovský, D. J. Millener, F. Garibaldi, and G. M. Urciuoli, *Electroproduction of p-shell hypernuclei in DWIA*, AIP Conference Proceedings **2130**, 020014 (2019), https://doi.org/10.1063/1.5118382

[8] M. D. Schwartz, *Quantum Field Theory and the Standard Model*, Cambridge University Press, 3/2014, ISBN 978-1-107-03473-0.

[9] S. Boffi, C. Giusti, F. D. Pacati, and M. Radici, *Electromagnetic Response of Atomic Nuclei*, Oxford University Press, 1996, ISBN 0-19-851774-2.

[10] N. Dombey, *Scattering of polarized leptons at high energy*, Rev. Mod. Phys. **41** (1969), 236-246 doi:10.1103/RevModPhys.41.236

[11] E. Amaldi, S. Fubini and G. Furlan, *Pion Electroproduction. Electroproduction at low-energy and hadron form-factors*, Springer Tracts Mod. Phys. **83** (1979), 1-162 doi:10.1007/BFb0048209

[12] G. F. Chew, M. L. Goldberger, F. E. Low and Y. Nambu, *Relativistic dispersion relation approach to photomeson production*, Phys. Rev. **106** (1957), 1345-1355 doi:10.1103/PhysRev.106.1345

[13] R. A. Adelseck and B. Saghai, *Kaon photoproduction: Data consistency, coupling constants, and polarization observables*, Phys. Rev. C **42** (1990), 108-127 doi:10.1103/PhysRevC.42.108

[14] B. B. Deo and A. K. Bisoi, *Pseudoscalar versus pseudovector interactions in photoproduction and electroproduction of charged mesons*, Phys. Rev. D **9** (1974), 288-295 doi:10.1103/PhysRevD.9.288

[15] R. A. Williams, C. R. Ji and S. R. Cotanch, *Hyperon electroproduction in a crossing and duality constrained model*, Phys. Rev. C **46** (1992), 1617-1635 doi:10.1103/PhysRevC.46.1617

[16] T. Mart, *Electromagnetic production of kaon near threshold*, Phys. Rev. C **82** (2010), 025209 doi:10.1103/PhysRevC.82.025209 [arXiv:1007.5366 [nucl-th]].

[17] D. Skoupil, *Electromagnetic production of kaons*, PhD diss., Czech Technical University in Prague, 2016

[18] D. Skoupil, and P. Bydžovský, *$K^+\Lambda$ photo- and electroproduction off proton*, AIP Conference Proceedings **2249**, 030042 (2020), https://doi.org/10.1063/5.0008575

[19] T. Mart and T. Wijaya, *Extending isobar model for kaon photoproduction up to 16-GeV*, Acta Phys. Polon. B **34** (2003), 2651-2664

[20] T. Mart, *Kaon photoproduction in field theoretic and multipoles approaches*, AIP Conference Proceedings **1862**, 020001 (2017), https://doi.org/10.1063/1.4991104

[21] G. Knochlein, D. Drechsel and L. Tiator, *Photoproduction and electroproduction of eta mesons*, Z. Phys. A **352** (1995), 327-343 doi:10.1007/BF01289506 [arXiv:nucl-th/9506029 [nucl-th]].

[22] V. Pascalutsa, *Quantization of an interacting spin - 3/2 field and the Δ isobar*, Phys. Rev. D **58** (1998), 096002 doi:10.1103/PhysRevD.58.096002 [arXiv:hep-ph/9802288 [hep-ph]].

[23] T. Vrancx, L. De Cruz, J. Ryckebusch and P. Vancraeyveld, *Consistent interactions for high-spin fermion fields*, Phys. Rev. C **84** (2011), 045201 doi:10.1103/PhysRevC.84.045201 [arXiv:1105.2688 [nucl-th]].

[24] K. Ohta, *Electromagnetic interactions of extended nucleons*, Phys. Rev. C **40** (1989), 1335–1346 doi:10.1103/PhysRevC.40.1335

[25] H. Haberzettl, *Gauge invariant theory of pion photoproduction with dressed hadrons*, Phys. Rev. C **56** (1997), 2041-2058 doi:10.1103/PhysRevC.56.2041 [arXiv:nucl-th/9704057 [nucl-th]].

[26] T. Mart and C. Bennhold, *Evidence for a missing nucleon resonance in kaon photoproduction*, Phys. Rev. C **61** (2000), 012201 doi:10.1103/PhysRevC.61.012201 [arXiv:nucl-th/9906096 [nucl-th]].

[27] T. Mart, C. Bennhold, H. Haberzettl, and L. Tiator, *Kaon-MAID Portal*, http://portal.kph.uni-mainz.de/MAID//kaon/kaonmaid.html

[28] S. Capstick and W. Roberts, *Quark models of baryon masses and decays*, Prog. Part. Nucl. Phys. **45** (2000), S241-S331 doi:10.1016/S0146-6410(00)00109-5 [arXiv:nucl-th/0008028 [nucl-th]].

[29] M. Q. Tran *et al.* [SAPHIR], *Measurement of $\gamma p \to K^+\Lambda$ and $\gamma p \to K^+\Sigma^0$ at photon energies up to 2 GeV*, Phys. Lett. B **445** (1998), 20-26 doi:10.1016/S0370-2693(98)01393-8

[30] K. H. Glander, J. Barth, W. Braun, *et al.* [SAPHIR], *Measurement of $\gamma p \to K^+\Lambda$ and $\gamma p \to K^+\Sigma^0$ at photon energies up to 2.6 GeV*, Eur. Phys. J. A **19** (2004), 251–273 https://doi.org/10.1140/epja/i2003-10119-x

[31] R. Bradford *et al.* [CLAS], *Differential cross sections for $\gamma + p \to K^+ + Y$ for Λ and Σ^0 hyperons*, Phys. Rev. C **73** (2006), 035202 doi:10.1103/PhysRevC.73.035202 [arXiv:nucl-ex/0509033 [nucl-ex]].

[32] M. Froissart, *Asymptotic behavior and subtractions in the Mandelstam representation*, Phys. Rev. **123** (1961), 1053-1057 doi:10.1103/PhysRev.123.1053

[33] P. Vancraeyveld, L. De Cruz, J. Ryckebusch and T. Vrancx, *Bayesian inference of the resonance content of $p(\gamma, K^+)\Lambda$*, EPJ Web Conf. **37** (2012), 08001 doi:10.1051/epjconf/20123708001 [arXiv:1208.3618 [nucl-th]].

[34] T. Mart and A. Sulaksono, *Kaon photoproduction in a multipole approach*, Phys. Rev. C **74** (2006), 055203 doi:10.1103/PhysRevC.74.055203 [arXiv:nucl-th/0609077 [nucl-th]].

[35] K. A. Olive *et al.* [Particle Data Group], *Review of Particle Physics*, Chin. Phys. C **38** (2014), 090001 doi:10.1088/1674-1137/38/9/090001

[36] R. Szmytkowski, *Recurrence and differential relations for spherical spinors*, J. Math. Chem. **42** (2007), 397-413 doi:10.1007/s10910-006-9110-0 [arXiv:1011.3433 [math-ph]].

[37] G. Niculescu, *et al.*, *Longitudinal and transverse cross-sections in the* $^1H(e,e'K^+)\Lambda$ *reaction*, Phys. Rev. Lett. **81** (1998), 1805-1808 doi:10.1103/PhysRevLett.81.1805

[38] R. M. Mohring *et al.* [E93018], *Separation of the longitudinal and transverse cross-sections in the* $p(e,e'K^+)\Lambda$ *and* $p(e,e'K^+)\Sigma^0$ *reactions*, Phys. Rev. C **67** (2003), 055205 doi:10.1103/PhysRevC.67.055205 [arXiv:nucl-ex/0211005 [nucl-ex]].

[39] P. Brauel, T. Canzler, D. Cords, R. Felst, G. Grindhammer, M. Helm, W. D. Kollmann, H. Krehbiel and M. Schadlich, *Electroproduction of* π^+n, π^-p *and* $K^+\Lambda$, $K^+\Sigma^0$ *Final States Above the Resonance Region*, Z. Phys. C **3** (1979), 101 doi:10.1007/BF01443698

[40] A. Bleckmann, S. Herda, U. Opara, W. Schulz, W. J. Schwille and H. Urbahn, *Photoproduction of* $K^+\Lambda$ *and* $K^+\Sigma^0$ *from hydrogen between 1.3 and 1.45 GeV*, Z. Phys. **239** (1970), 1-15 doi:10.1007/BF01408507

[41] G. P. Lepage, *A New Algorithm for Adaptive Multidimensional Integration*, J. Comput. Phys. **27** (1978), 192 doi:10.1016/0021-9991(78)90004-9

[42] B. D. Serot and J. D. Walecka, *The Relativistic Nuclear Many Body Problem*, Adv. Nucl. Phys. **16** (1986), 1-327 ITP-740-STANFORD.

[43] G. A. Lalazissis, J. Konig and P. Ring, *A New parametrization for the Lagrangian density of relativistic mean field theory*, Phys. Rev. C **55** (1997), 540-543 doi:10.1103/PhysRevC.55.540 [arXiv:nucl-th/9607039 [nucl-th]].

[44] B. G. Todd-Rutel and J. Piekarewicz, *Neutron-Rich Nuclei and Neutron Stars: A New Accurately Calibrated Interaction for the Study of Neutron-Rich Matter*, Phys. Rev. Lett. **95** (2005), 122501 doi:10.1103/PhysRevLett.95.122501 [arXiv:nucl-th/0504034 [nucl-th]].

Appendices

Appendix A

Identities for Dirac matrices

This appendix contains a few identities involving Dirac matrices that are useful to simplify some types of calculations encountered in this work.

A.1 Dirac algebra

$$\{\gamma^\mu, \gamma^\nu\} = 2g^{\mu\nu} \tag{A.1}$$

$$\gamma^5 = i\gamma^0\gamma^1\gamma^2\gamma^3 \tag{A.2}$$

$$(\gamma^5)^2 = \mathbb{1} \tag{A.3}$$

$$\{\gamma^\mu, \gamma^5\} = 0 \tag{A.4}$$

A.2 Trace identities

$$tr(\text{odd number of } \gamma^\alpha) = 0 \tag{A.5}$$

$$tr(\gamma^\alpha\gamma^\beta) = 4g^{\alpha\beta} \tag{A.6}$$

$$tr(\gamma^\alpha\gamma^\beta\gamma^\gamma\gamma^\delta) = 4(g^{\alpha\beta}g^{\gamma\delta} + g^{\alpha\delta}g^{\gamma\beta} - g^{\alpha\gamma}g^{\beta\delta}) \tag{A.7}$$

$$tr\gamma^5 = tr(\gamma^5\gamma^\alpha\gamma^\beta) = 0 \tag{A.8}$$

$$tr(\gamma^5 \cdot \text{odd number of } \gamma^\alpha) = 0 \tag{A.9}$$

$$tr(\gamma^5\gamma^\alpha\gamma^\beta\gamma^\gamma\gamma^\delta) = -4i\epsilon^{\alpha\beta\gamma\delta} \tag{A.10}$$